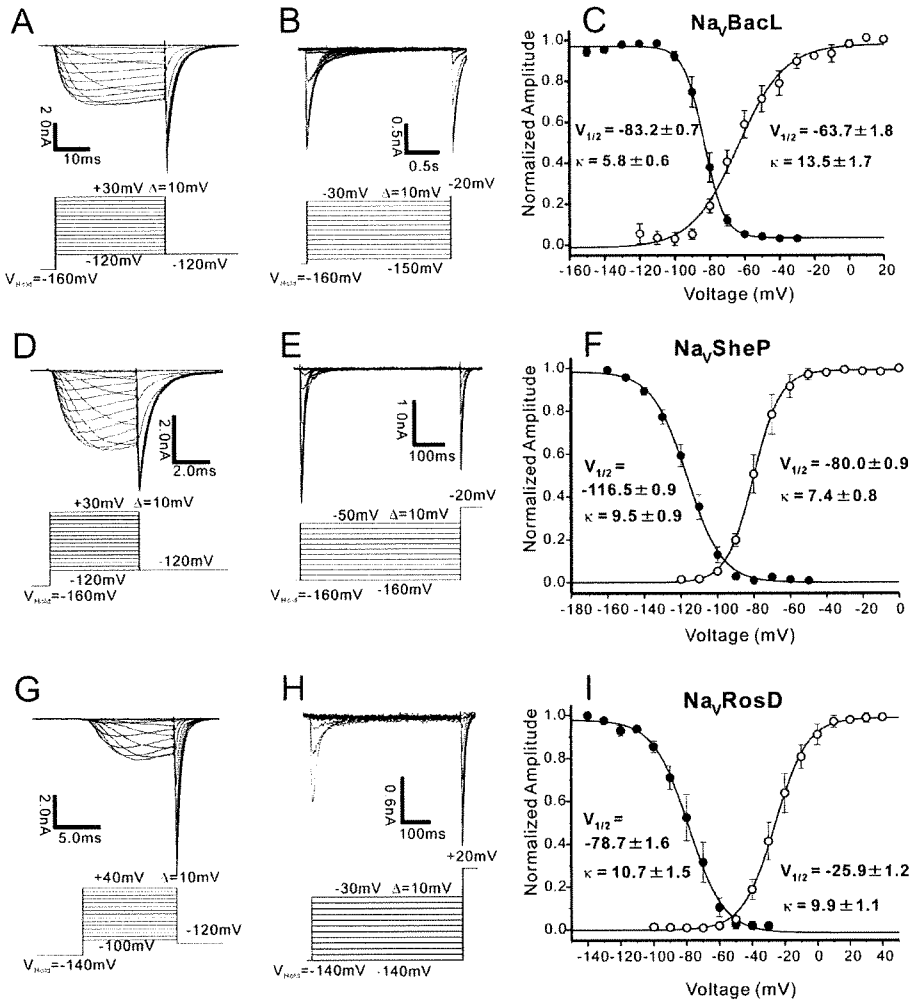

FIGURE 4. **Voltage-dependent activation and inactivation of Na_VBacL, Na_VSheP, and Na_VRosD.** *A*, $I_{NaVBacL}$ deactivation tail currents. After prepulses of varying depolarization (from −120 to +30 mV, increments of +10 mV), tail currents were measured at −120 mV. *B*, $I_{NaVBacL}$ steady-state inactivation currents. After a 2-s prepulse, the channels inactivated to a steady-state level and were reactivated by a second depolarizing pulse (−20 mV). *C*, $I_{NaVBacL}$-normalized activation curve (*open circle*, $n = 9$; ±S.E.) and steady-state inactivation curve (closed circle, $n = 9$; ±S.E.). *D*, $I_{NaVSheP}$ deactivation tail currents. After prepulses of varying depolarization (from −120 to +30 mV, increments of +10 mV), tail currents were measured at −120 mV. *E*, $I_{NaVSheP}$ steady-state inactivation currents. After a 500-ms prepulse, the channels inactivated to a steady-state level and were reactivated by a second depolarizing pulse (−20 mV). *F*, $I_{NaVSheP}$-normalized activation curve (*open circle*, $n = 6$; ±S.E.) and steady-state inactivation curve (*closed circle*, $n = 6$; ±S.E.). *G*, $I_{NaVRosD}$ deactivation tail currents. After prepulses of varying depolarization (from −100 to +40 mV, increments of +10 mV), tail currents were measured at −120 mV. *H*, $I_{NaVRosD}$ steady-state inactivation currents. After a 500-ms prepulse, the channels inactivated to a steady-state level and were reactivated by a second depolarizing pulse (+20 mV). *I*, $I_{NaVRosD}$-normalized activation curve (*open circle*, $n = 6$; ±S.E.) and steady-state inactivation curve (*closed circle*, $n = 6$; ±S.E.). The voltages with half-inactivation/activation and the slope factors are indicated as $V_{1/2}$ (mV) and κ (mV/e-fold), respectively in *C*, *F*, and *I*. The intersweep interval was 15 s in *A*, *B*, *D*, *E*, *G*, and *H*.

homologues, six of them were commercially available: *B. licheniformis*, isolated from soil and plant material (27), and *L. vestfoldensis* (28), *R. sphaeroides* (29), *S. putrefaciens* (30), *R. denitrificans* (31), and *Oceanicaulis* sp. (32) isolated from sea water (28–33). Using the colony-direct PCR method, we were able to clone the putative Na_V genes from three of these six bacteria, namely from *B. licheniformis*, *S. putrefaciens*, and *R. denitrificans*.

Sequencing of the Na_VBacL gene from *B. licheniformis* revealed an open reading frame of 276 amino acids with a predicted molecular size of 31.8 kDa, and sequencing of the Na_VRosD gene from *R. denitrificans* showed an open reading frame of 259 amino acids (29.2 kDa). Both sequences were identical with the deposited sequences. Our sequence of the Na_VSheP gene from *S. putrefaciens*, encoding an open reading frame of 295 amino acids (33.1 kDa), differed, however, from the sequence deposited in the GenBank™ data base in several places (T31A, A54T, V62L, and N88S) (Fig. 2*A*). Na_VBacL, Na_VSheP, and Na_VRosD share with NaChBac sequence identities (sequence similarities) of 49% (57%), 32% (44%), and 37% (48%), respectively, and hydropathy plots predict a six-transmembrane architecture for all three proteins (Fig. 2*A*).

C-terminally His-tagged constructs of all three Na_Vs expressed well in *E. coli* and could be purified by metal chelate affinity chromatography (Fig. 2*B*). Na_VBacL and Na_VRosD migrated as a single band on SDS-polyacrylamide gels (~34 and ~25 kDa, respectively), whereas Na_VSheP migrated mainly as a ~35 kDa band but also showed additional smaller bands. The smaller bands could also be detected on Western blots probed with anti-His antibodies (data not shown). Mass spectra confirmed that all main bands represented the full-length proteins and identified the molecular masses of the smaller bands of Na_VSheP as 22,662 and 23,053 Da (Fig. 2*C*). The additional bands thus represent C-terminal fragments of Na_VSheP that were generated by cleavage of the carboxyl group of residues Arg^{110}, the first arginine of helix S4, and Ala^{107} (Fig. 2*A*).

We transfected mammalian cell lines (CHO-K1 or HEK 293) with the genes encoding Na_VBacL, Na_VSheP, and Na_VRosD and measured the resulting currents (Fig. 3). Although no currents were observed in non-transfected or mock-transfected cells (data not shown), currents could be recorded from cells transfected with the Na_V genes, and all three channels required at least 1 s for 90% recovery from inactivation. Cells transfected with each of the three Na_Vs exhibited large voltage-activated inward currents of up to 10 nA (Fig. 3, *A–C*), peaking at −40, −50, and −10 mV for Na_VBacL, Na_VSheP, and Na_VRosD, respectively (Fig. 3, *D–F*). The reversal potential of Na_VRosD-mediated current ($I_{NaVRosD}$) was

+42.7 mV in a bath solution containing 150 mM Na^+. The inward currents produced by Na_VBacL and Na_VSheP in a bath solution containing 150 mM Na^+ were, however, peaking at a membrane potential that was too low to clamp the membrane potentials at low voltage. To measure the currents produced by Na_VBacL and Na_VSheP, we therefore reduced the NaCl concentration in the bath solution from 150 to 75 mM and added instead 75 mM *N*-methyl-D-glucamine. The reversal potential of $I_{NaVBacL}$ and $I_{NaVSheP}$ could then be determined as +28.3 and +33.0 mV, respectively. Ion substitution (Ca^{2+}, K^+, and *N*-methyl-D-glucamine replacement) confirmed that all three proteins form Na^+-selective channels and that they are sensitive to high concentrations of nifedipine (30 μM) (data not shown). Their pharmacological sensitivity closely resembles that of L-type Ca_Vs, as already reported for the previously characterized homologues (5–7).

$I_{NaVBacL}$ was activated with a time constant ($\tau_{activation}$) of 4.92 ± 0.73 ms at +10 mV (n = 15) and inactivated with $\tau_{inactivation}$ of 96.1 ± 9.60 ms at +10 mV (n = 15). Both time constants were significantly larger than those of mammalian Na_V channels ($\tau_{activation}$ = 2 ms; $\tau_{inactivation}$ = 10 ms) but faster than those of $I_{NaChBac}$ ($\tau_{activation}$ = 12.9 ms; $\tau_{inactivation}$ = 166 ms) (5). $I_{NaVSheP}$ ($\tau_{activation}$ = 0.89 ± 0.076 ms at −10 mV, n = 17; $\tau_{inactivation}$ = 9.90 ± 0.57 ms at −10 mV, n = 17) and $I_{NaVRosD}$ ($\tau_{activation}$ = 1.61 ± 0.12 ms at +20 mV, n = 15; $\tau_{inactivation}$ = 9.88 ± 1.25 ms at +20 mV, n = 15) were activated and inactivated significantly faster than $I_{NaVBacL}$ and $I_{NaChBac}$. Remarkably, the time constants of them were as small as those of the α-subunit of the rat skeletal muscle-type Na_V (34).

We evaluated the voltage-dependent activation of Na_VBacL by measuring deactivation tail currents (Fig. 4*A*). A Boltzmann fit of the averaged activation curve yielded an activating potential of 50% activation ($V_{½}$) of −63.7 ± 1.8 mV (n = 9) and a slope factor (κ) of 13.5 ± 1.7 mV/e-fold change in current (Fig. 4*C*). The steady-state inactivation of the channel was determined by sequential depolarization to test voltages, followed by voltage clamp to the peak of activation at −20 mV (Fig. 4*B*). Steady-state inactivation was a steep function of voltage, with 50% inactivation at −83.2 ± 0.7 mV (n = 9) and κ = 5.8 ± 0.6 mV/e-fold change (Fig. 4*C*). Although Na_VBacL had similar time constants of activation and inactivation as NaChBac (5), Na_VBacL activated and inactivated at voltages about 40 mV lower than those of NaChBac (Table 1).

Boltzmann fits of their activation curves yielded $V_{½}$ of −80.0 ± 0.9 mV and κ of 7.4 ± 0.8 mV/e-fold change for Na_VSheP (n = 6; Fig. 4, *D* and *F*) and $V_{½}$ of −25.9 ± 1.2 mV and κ of 9.9 ± 1.1 mV/e-fold change for Na_VRosD (n = 6; Fig. 4, *G* and *I*). The steady-state inactivation of Na_VSheP and Na_VRosD were dependent on the voltage with half-inactivations at −116.5 ± 0.9 mV (κ = 9.5 ± 0.9 mV/e-fold) (n = 6; Fig. 4, *E* and *F*) and −78.7 ± 1.6 mV (κ = 10.7 ± 1.6 mV/e-fold) (n = 6; Fig. 4, *H* and *I*), respectively. Na_VSheP activated and inactivated at the lowest membrane potential of all NaChBac homologues studied to date. The voltage dependences of the three prokaryotic Na_Vs analyzed in this study are summarized in Table 1.

Previous studies indicated that a glycine residue in the middle of helix S6, named the "glycine hinge," is critical for gating of tetrameric cation channels (15–17). A glycine residue corresponding to the glycine hinge is present in NaChBac (Gly^{219}) but not in Na_VBacL (Ala^{214}), Na_VSheP (Ala^{216}), and Na_VRosD (Thr^{207}) (*red arrow* in Fig. 5*A*). Other glycine residues in Na_VBacL (Gly^{224}), Na_VRosD (Gly^{217}), and also NaChBac (Gly^{229}) are found in the lower part of helix S6. This part is near the cytoplasmic side and corresponds to the position of the PXP motif, a Pro-*X*-Pro or glycine motif that is important for gating in hERG (human ether-a-go-go related gene) and K_V channels (18, 19) (*green arrow* in Fig. 5*A*) and creates a kink in helix S6 of K_V1.2 (Fig. 5*C*). By contrast, Na_VSheP contains no glycine residues in helix S6 (Fig. 5*A*).

TABLE 1

$V_{½}$ of inactivation and activation of prokaryotic Na_Vs

$V_{½}$ of inactivation is the membrane potential of 50% steady-state inactivation. $V_{½}$ of activation is the potential of 50% activation. All results are expressed as mean ± S.E. All experiments were performed at pH 7.4 except for the indicated experiment at pH 9.0.

	$V_{½}$		Note
	Inactivation	Activation	
	mV		
Na_VBacL	−83.2 ± 0.7	−63.7 ± 1.8	n = 9
Na_VSheP	−116 ± 0.9	−80.0 ± 0.9	n = 6
Na_VRosD	−78.7 ± 1.6	−25.9 ± 1.2	n = 6
NaChBac	−40	−24	Ref. 5
Na_VPZ	−35	−10	Ref. 7
Na_VSP	−22	21	Ref. 7
Na_VBP	−57	−35	Ref. 6
	−86	−64	At pH 9.0

To evaluate their role, we mutated the glycines in helix S6 of Na_VBacL, Na_VRosD, and NaChBac to alanine, a residue known to strongly stabilize α-helical secondary structure (35). All mutants retained the channel currents, but their time constants of inactivation changed significantly. On the other hand, their activation rates and also voltage dependences were less influenced by the mutations. Table 2 summarizes the $\tau_{activation}$ and $\tau_{inactivation}$ values of all analyzed mutant and wild-type channels as well as the statistical differences in $\tau_{inactivation}$ between the wild-type channels and the various mutants. As a control, we made an alanine substitution of residue Gly^{201} in Na_VBacL, which is located in the pore-S6 loop (*blue arrow* in Fig. 5*A*). This mutation had no effect on the time constant of inactivation (Table 2). With $\tau_{inactivation}$ of 21.4 ± 2.19 ms at +10 mV, the NaChBac G219A mutant showed faster inactivation than wild-type NaChBac ($p < 0.01$) (Fig. 5*D*). NaChBac G229A ($\tau_{inactivation}$ = 230 ± 33.8 ms at +10 mV), Na_VBacL G224A ($\tau_{inactivation}$ = 270 ± 53.3 ms at +10 mV), and Na_VRosD G217A ($\tau_{inactivation}$ = 60.9 ± 13.0 ms at +20 mV) showed significantly slower inactivation than the corresponding wild-type channels ($p < 0.01$) (Fig. 5, *D–F*). Inactivation of the NaChBac G219A/G229A double mutant ($\tau_{inactivation}$ = 156 ± 16.2 ms at +10 mV) showed no statistically relevant difference compared with the inactivation of the wild-type protein and was significantly slower than that of NaChBac G219A (Fig. 5*D*). All mutants lacking glycine residues in helix S6 still showed activation and inactivation.

Na_VBacL, Na_VSheP, and Na_VRosD do not have a glycine at the position that corresponds to the glycine hinge in helix S6. When the residues in this position were mutated to glycine, the mutants, with the exception of Na_VRosD T207G (see below), also produced measurable inward currents (more than 1 nA) (Fig. 5,

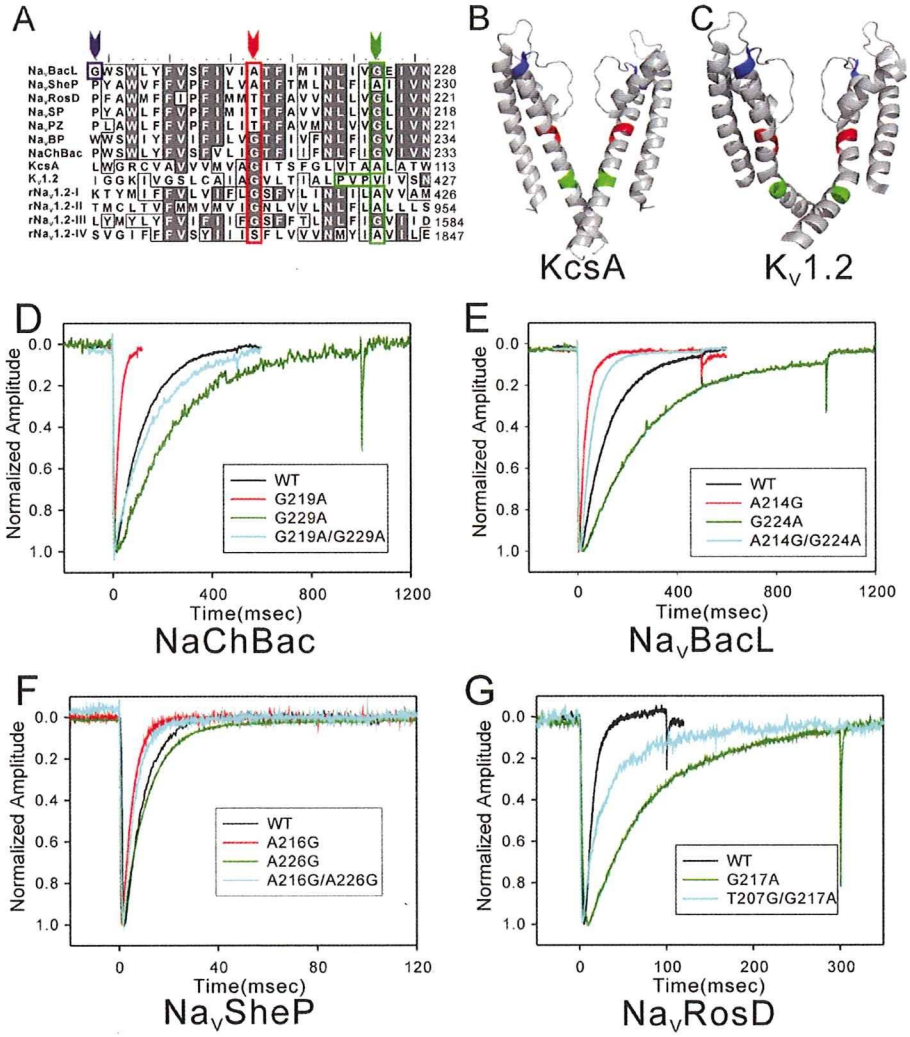

FIGURE 5. **Electrophysiological analysis of the effects of mutations in helix S6.** *A*, alignment of helix S6 and inner helix sequences of Na_VBacL, Na_VSheP, Na_VRosD, Na_VSP, Na_VPZ, Na_VBP, NaChBac, KcsA (potassium channel from *Streptomyces lividans*), K_V1.2 (potassium channel from *Rattus norvegicus*), and the four subdomains (I–IV) of Na_V1.2 (voltage-gated sodium channel from rat brain). The *arrowheads* indicate the positions of G201 in Na_VBacL (*blue*), the glycine hinge (*red*), and the PXP motif (*green*); residues of these motifs are *boxed* in the corresponding *colors*. *B* and *C*, *ribbon diagrams* of KcsA (Protein Data Bank code 1r3j) (*B*) and K_V1.2 (Protein Data Bank code 2r9r) (*C*) with the residues and motifs described in *A* shown in the same *colors*. *D*, representative traces of currents produced by wild-type and mutant NaChBac channels activated by the following voltage protocol. After holding the potential at −120 mV, currents were measured at +10 mV for 500 ms (wild type (*WT*) and G219A/G229A), 100 ms (G219A), and 1 s (G229A). *E*, representative traces of currents produced by wild-type and mutant Na_VBacL channels activated by the following voltage protocol. After holding the potential at −160 mV, currents were measured at +10 mV for 500 ms (wild type, A214G, and A214G/G224A) and 1 s (G224A). *F*, representative traces of currents produced by wild-type and mutant Na_VSheP channels activated by the following voltage protocol. After holding the potential at −160 mV, currents were measured at −10 mV for 100 ms. *G*, representative traces of currents produced by wild-type and mutant Na_VRosD channels activated by the following voltage protocol. After holding the potential at −140 mV, currents were measured at +20 mV for 100 ms (wild type) and 300 ms (G217A and T207G/G217A).

D–F). Furthermore, Na_VBacL A214G ($\tau_{inactivation}$ = 29.5 ± 3.14 ms at +10 mV) and Na_VSheP A216G ($\tau_{inactivation}$ = 5.35 ± 0.72 ms at −10 mV) showed significantly faster inactivation than the respective wild-type channels ($p < 0.01$) (Fig. 5, *E–G*). Na_VRosD T207G showed only a small and fast inactivated current (~200 pA; $\tau_{inactivation} < 2$ ms). Because HEK293 or CHO-K1 cells express endogenous sodium channels that produce similar small currents (36), the current produced by the Na_VRosD T207G mutant could not be distinguished from that produced by the endogenous sodium channels. Ala^{226} of Na_VSheP is the residue in the region in the lower part of helix S6 that corresponds to the PXP motif in voltage-dependent potassium channels (*green arrow* in Fig. 5*A*). The inactivation rate of Na_VSheP A226G ($\tau_{inactivation}$ = 11.6 ± 0.50 ms at −10 mV) was slightly slower than that of the wild-type channel, but the difference is not statistically significant (Fig. 5*F*). Double mutation of two residues also retained the inward current of sodium ions. The inactivation rate of Na_VBacL A214G/G224A ($\tau_{inactivation}$ = 54.1 ± 4.51 ms at +10 mV, n = 9) was significantly faster than that of Na_VBacL G224A ($p < 0.01$) and slower than that of Na_VBacL A214G, although the difference was not statistically significant (Fig. 5*E*). Na_VSheP A216G/A226G ($\tau_{inactivation}$ = 7.61 ± 0.65 ms at −10 mV) inactivated as fast as Na_VSheP A216G. Na_VRosD T207G/G217A ($\tau_{inactivation}$ = 20.93 ± 3.90 ms at +20 mV) produced a current less than 500 pA. This current could be distinguished from that of endogenous sodium channels and showed a faster inactivation than Na_VRosD G217A ($p < 0.01$). In summary, mutations of the residues corresponding to the glycine hinge accelerated the inactivation rate, mutations of glycines in the lower part of helix S6 to alanine reduced the inactivation rate, and the A226G mutation in Na_VSheP had no effect on the inactivation rate.

DISCUSSION

We cloned three new NaChBac homologues from *B. licheniformis*, *S. putrefaciens*, and *R. denitrificans*. The three channels differ in their kinetics and voltage dependences, which may reflect differences in the environment in which the respective bacteria live. The physiological role of the Na_V homologue found in the alkaliphilic bacterium *Bacillus pseudofirmus*, Na_VBP, has been well studied (6, 12). Deletion of Na_VBP resulted in impaired pH homeostasis and reversed pH chemotaxis (6). These results suggest that Na_VBP functions in conjunction with the multiple resistance and pH adaptation Na^+/H^+ antiporter in pH homeostasis, with the sodium-driven motor protein complex in motility (6), and with the methyl-accepting chemotaxis

TABLE 2

Time constants of activation and inactivation of prokaryotic Na_Vs

The time constant of activation ($\tau_{activation}$) is the time from 10 to 90% of peak current. The time constant of inactivation ($\tau_{inactivation}$) is the time from peak current to 1/e of peak current. All results are expressed as mean ± S.E. The statistical significance of differences in $\tau_{inactivation}$ of each mutant compared to wild-type protein or other mutants is shown in the column, "Statistical significance of $\tau_{inactivation}$." $\tau_{activation}$ and $\tau_{inactivation}$ of NaChBac, Na_VBacL, Na_VSheP, and Na_VRosD were measured at +10, +10, −10, and +20 mV, respectively. All experiments were performed at pH 7.4. To assess statistical differences in $\tau_{inactivation}$ between wild type and mutant proteins, multiple comparisons were made by one-way analysis of variance followed by the Tukey-Kramer multiple comparisons test. NS, not significant.

	Time constant		Statistical significance of $\tau_{inactivation}$			No. of measurements
	$\tau_{activation}$	$\tau_{inactivation}$	WT	G219A	G229A	
	ms					
NaChBac	3.73 ± 0.73	118 ± 10.2				13
NaChBac G219A	0.95 ± 0.22	21.4 ± 2.19	$p < 0.01$			5
NaChBac G229A	12.0 ± 3.33	230 ± 33.8	$p < 0.01$	$p < 0.01$		5
NaChBac G219A/G229A	2.86 ± 0.47	156 ± 16.2	NS	$p < 0.01$	$p < 0.05$	11
			WT	A214G	G224A	
Na_VBacL	4.92 ± 0.73	96.1 ± 9.60				15
Na_VBacL A214G	1.70 ± 0.27	29.5 ± 3.14	$p < 0.01$			11
Na_VBacL G224A	3.69 ± 1.21	270 ± 53.3	$p < 0.01$	$p < 0.01$		5
Na_VBacL A214G/G224A	4.63 ± 0.57	54.1 ± 4.51	NS	NS	$p < 0.01$	9
Na_VBacL G201A	2.20 ± 0.32	81.0 ± 12.6	NS[a]			7
			WT	A216G	G226A	
Na_VSheP	0.89 ± 0.076	9.90 ± 0.57				17
Na_VSheP A216G	0.82 ± 0.10	5.35 ± 0.72	$p < 0.01$			8
Na_VSheP A226G	0.85 ± 0.08	11.6 ± 0.50	NS	$p < 0.01$		9
Na_VSheP A216G/A226G	0.87 ± 0.10	7.61 ± 0.65	$p < 0.05$	NS	$p < 0.01$	10
			WT	G217A		
Na_VRosD	1.61 ± 0.12	9.88 ± 1.25				15
Na_VRosD G217A	2.06 ± 0.45	60.9 ± 13.0	$p < 0.01$			7
Na_VRosD T207G/G217A	2.92 ± 0.63	20.93 ± 3.90	NS	$p < 0.01$		6

[a] A simple comparison between Na_VBacL wild type and G201A was made by Student's *t* test.

proteins in chemotaxis (12). Multiple resistance and pH adaptation antiporters (37), sodium-driven motor protein complex (38), and methyl-accepting chemotaxis proteins (39) are found in many bacteria, and prokaryotic Na_Vs might thus play the same roles in other bacteria as Na_VBP in *B. pseudofirmus*.

Because bacteria live in environments that differ in pH, temperature, and ionic conditions, it seems reasonable that they express Na_Vs with channel properties that have adapted to their specific environments. First, activation and inactivation of prokaryotic Na_Vs cloned from marine bacteria (Na_VSP, Na_VSheP, and Na_VRosD but not Na_VPZ) were faster than those of homologues cloned from *Bacillus* species (NaChBac, Na_VBP, and Na_VBacL) (Table 2). Marine bacteria live in an environment with a higher concentration of sodium ions than soil bacteria, such as *Bacillus* species. The fast inactivation of Na_Vs found in marine bacteria might thus be an adaptation that evolved to prevent the influx of excess sodium ions into the cytoplasm. Second, although Na_VBacL and Na_VBP, both expressed in *Bacillus* species isolated from soil, have similar kinetics of activation and inactivation, their voltage dependences differ from each other. At the neutral pH of 7.4, half of Na_VBP is activated by a voltage of −35 mV and inactivated by a voltage of −57 mV (6) (Table 1). These membrane potentials are 30 mV higher than those that activate and inactivate Na_VBacL. At pH 9.0, the pH of the environment in which *B. pseudofirmus* lives, half of Na_VBP is, however, activated by a voltage of −64 mV and inactivated by a voltage of −86 mV (6). Hence, at the pH of the environment in which the respective bacterium lives, the two channels have similar voltage dependences of activation and inactivation. This finding suggests that the channel characteristics of prokaryotic Na_Vs have been optimized for the specific environments of the bacteria.

The diversity in the channel properties of prokaryotic Na_Vs can help us to obtain a better understanding of the molecular mechanisms that underlie ion channel function. The crystal structure of the $K_V1.2/K_V2.1$ chimera potassium channel suggested that the S4-S5 linker helix pushes down on the lower part of helix S6 and thus keeps the ion pore closed in the resting state (13). A single molecule study demonstrated that this region of KcsA is rotated in the open state (40) and thus confirmed that this region works as an activation gate. If the pore domain were folded tightly, such as seen in crystal structures of potassium channels, the role of the glycine hinge and the PXP motif in channel gating might be to provide sufficient flexibility to allow the lower part of helix S6 to bend and move for activation. On the other hand, prokaryotic Na_V mutants lacking glycine and proline residues in helix S6 and wild-type Na_VSheP still show activation and inactivation (Fig. 5 and Table 2). Neither motif can thus be essential for gating in prokaryotic Na_Vs. Because bending of helix S6 would be difficult without such gating motifs, it is likely that in these mutants and in wild-type Na_VSheP, the entire helix S6 has to incline to open the activation gate. Therefore, it is likely that the pore domain of prokaryotic Na_Vs is folded more loosely to increase the mobility of helix S6.

Inactivation of prokaryotic Na_Vs is thought to occur through the C-type inactivation mechanism seen in other tetrameric cation channels. C-type inactivation has been explained by conformational changes around the selectivity filter of the channel (23–25). These conformational changes, which cause the selectivity filter to collapse, act as an inactivation gate. Therefore, the stability of the selectivity filter could affect the rate of C-type inactivation. In the case of KcsA, it has been proposed that the residues adjacent to Gly^{99}, which is the residue corresponding to the glycine hinge, interact with residues forming the bottom

of the selectivity filter, thus stabilizing its conductive conformation (41). This motif of $K_v1.2$ also locates beside the selectivity filter (Fig. 5, *B* and *C*). Based on the similarity of the primary sequences, the corresponding region in prokaryotic Na_Vs would also be near their selectivity filters. All mutations in this region in Na_VBacL (A214G), Na_VSheP (A216G), Na_VRosD (T207G), and also NaChBac (G219A) accelerated the inactivation rate. Remarkably, the T207G mutation reduced ion currents in Na_VRosD T207G and Na_VRosD T207G/G217A. These mutations would be expected to make the selectivity filter less stable and easier to collapse. As a result, the mutants would inactivate faster than the respective wild-type channels.

The lower part of helix S6 is thought to act as activation gate (13, 40). C-type inactivation always occurs after activation and thus appears to be coupled to activation. The coupling between the activation and inactivation gates is thought to be mediated by residues adjacent to the glycine hinge in helix S6 and the bottom of the selectivity filter (41). Our glycine-to-alanine mutations in the lower part of helix S6 reduced the inactivation rate. This result suggests that the glycine-to-alanine mutations, which stabilize the lower part of helix S6, weaken the coupling between the activation and inactivation gates and thus delay inactivation. Na_VSheP is the only channel in which the alanine-to-glycine mutation (A226G) showed no effect. It thus appears that although this region is important for the coupling in other channels, it may not have the same importance for coupling in Na_VSheP. This notion is supported by the fact that Na_VSheP lacks glycines in helix S6 and may thus use a coupling mechanism that in its details differs from that of other prokaryotic Na_Vs. In a previous report, a G219P mutation in NaChBac eliminated C-type inactivation (16). However, this glycine residue is not obligatory for activation gating. Therefore, the G219P mutation might force helix S6 to adopt an unusual bent conformation, in which helix S6 would not be able to mediate the coupling between the activation and inactivation gates.

Double mutations in the region corresponding to the glycine hinge and the lower part of helix S6 independently affected the inactivation rate in Na_VBacL, Na_VRosD, and NaChBac. It is possible that other regions in helix S6 are also involved in C-type inactivation. Nevertheless, the mutational results at these two regions may serve as useful footholds for the study of C-type inactivation. All mutations in this study had stronger effects on the inactivation rate than on the activation rate. The driving force for activation is depolarization, whereas C-type inactivation is due to the collapse of the selectivity filter, which depends on thermal instability. It is thus not unexpected that C-type inactivation is more sensitive to mutations than channel activation. Although these results provide first clues to the coupling of activation and inactivation in voltage-gated cation channels, a deep understanding of this phenomenon will require further mutational studies as well as the analysis of atomic structures.

Without knowing the three-dimensional structure of Na_V channels, it is impossible to understand the sodium selectivity of these channels and how small changes in their primary sequences result in different voltage dependences and gating kinetics. A high resolution structure is particularly crucial for understanding the structural basis of sodium selectivity. Because the three Na_Vs characterized in this study could be expressed at high levels and purified in large amounts, they are promising candidates for structural studies and thus increase the chances of obtaining a high resolution crystal structure.

Prokaryotic Na_Vs are the simplest voltage-gated cation channels known to date. They are composed of fewer than 300 amino acids, and differences in their channel characteristics are due to small changes in their primary sequences. As functional analyses proceed and structures become available, prokaryotic Na_Vs have the potential not only to reveal the basic molecular mechanisms of voltage-gated cation channels but also to provide insight into the molecular evolution of these channels.

Acknowledgments—We thank Dr. Chikara Sato (Advanced Industrial Science and Technology, Neuroscience Research Institute) for kindly providing NaChBac DNA and Drs. Christoph Gerle and Kentaro Noma for valuable discussions. We are grateful to Dr. Thomas Walz for critical reading of the manuscript.

REFERENCES

1. Hille, B. (2001) *Ion Channels of Excitable Membranes*, 3rd Ed., Sinauer Associates, Sunderland, MA
2. Catterall, W. A. (1992) *Physiol. Rev.* **72,** S15–S48
3. Catterall, W. A. (1995) *Annu. Rev. Biochem.* **64,** 493–531
4. Sato, C., Ueno, Y., Asai, K., Takahashi, K., Sato, M., Engel, A., and Fujiyoshi, Y. (2001) *Nature* **409,** 1047–1051
5. Ren, D., Navarro, B., Xu, H., Yue, L., Shi, Q., and Clapham, D. E. (2001) *Science* **294,** 2372–2375
6. Ito, M., Xu, H., Guffanti, A. A., Wei, Y., Zvi, L., Clapham, D. E., and Krulwich, T. A. (2004) *Proc. Natl. Acad. Sci. U.S.A.* **101,** 10566–10571
7. Koishi, R., Xu, H., Ren, D., Navarro, B., Spiller, B. W., Shi, Q., and Clapham, D. E. (2004) *J. Biol. Chem.* **279,** 9532–9538
8. Doyle, D. A., Morais Cabral, J., Pfuetzner, R. A., Kuo, A., Gulbis, J. M., Cohen, S. L., Chait, B. T., and MacKinnon, R. (1998) *Science* **280,** 69–77
9. Jiang, Y., Lee, A., Chen, J., Ruta, V., Cadene, M., Chait, B. T., and MacKinnon, R. (2003) *Nature* **423,** 33–41
10. Jiang, Y., Lee, A., Chen, J., Cadene, M., Chait, B. T., and MacKinnon, R. (2002) *Nature* **417,** 515–522
11. Nurani, G., Radford, M., Charalambous, K., O'Reilly, A. O., Cronin, N. B., Haque, S., and Wallace, B. A. (2008) *Biochemistry* **47,** 8114–8121
12. Fujinami, S., Sato, T., Trimmer, J. S., Spiller, B. W., Clapham, D. E., Krulwich, T. A., Kawagishi, I., and Ito, M. (2007) *Microbiology* **153,** 4027–4038
13. Long, S. B., Tao, X., Campbell, E. B., and MacKinnon, R. (2007) *Nature* **450,** 376–382
14. Alam, A., and Jiang, Y. (2009) *Nat. Struct. Mol. Biol.* **16,** 30–34
15. Jiang, Y., Lee, A., Chen, J., Cadene, M., Chait, B. T., and MacKinnon, R. (2002) *Nature* **417,** 523–526
16. Zhao, Y., Yarov-Yarovoy, V., Scheuer, T., and Catterall, W. A. (2004) *Neuron* **41,** 859–865
17. Ding, S., Ingleby, L., Ahern, C. A., and Horn, R. (2005) *J. Gen. Physiol.* **126,** 213–226
18. Hardman, R. M., Stansfeld, P. J., Dalibalta, S., Sutcliffe, M. J., and Mitcheson, J. S. (2007) *J. Biol. Chem.* **282,** 31972–31981
19. Labro, A. J., Raes, A. L., Bellens, I., Ottschytsch, N., and Snyders, D. J. (2003) *J. Biol. Chem.* **278,** 50724–50731
20. Armstrong, C. M., and Bezanilla, F. (1977) *J. Gen. Physiol.* **70,** 567–590
21. Murrell-Lagnado, R. D., and Aldrich, R. W. (1993) *J. Gen. Physiol.* **102,** 949–975
22. Murrell-Lagnado, R. D., and Aldrich, R. W. (1993) *J. Gen. Physiol.* **102,** 977–1003
23. Ogielska, E. M., Zagotta, W. N., Hoshi, T., Heinemann, S. H., Haab, J., and Aldrich, R. W. (1995) *Biophys. J.* **69,** 2449–2457
24. Ong, B. H., Tomaselli, G. F., and Balser, J. R. (2000) *J. Gen. Physiol.* **116,**

653–662
25. Pavlov, E., Bladen, C., Winkfein, R., Diao, C., Dhaliwal, P., and French, R. J. (2005) *Biophys. J.* **89,** 232–242
26. Blunck, R., Starace, D. M., Correa, A. M., and Bezanilla, F. (2004) *Biophys. J.* **86,** 3966–3980
27. Rey, M. W., Ramaiya, P., Nelson, B. A., Brody-Karpin, S. D., Zaretsky, E. J., Tang, M., Lopez de Leon, A., Xiang, H., Gusti, V., Clausen, I. G., Olsen, P. B., Rasmussen, M. D., Andersen, J. T., Jørgensen, P. L., Larsen, T. S., Sorokin, A., Bolotin, A., Lapidus, A., Galleron, N., Ehrlich, S. D., and Berka, R. M. (2004) *Genome Biol.* **5,** R77
28. Van Trappen, S., Mergaert, J., and Swings, J. (2004) *Int. J. Syst. Evol. Microbiol.* **54,** 1263–1269
29. Choudhary, M., Zanhua, X., Fu, Y. X., and Kaplan, S. (2007) *J. Bacteriol.* **189,** 1914–1921
30. Ziemke, F., Höfle, M. G., Lalucat, J., and Rosselló-Mora, R. (1998) *Int. J. Syst. Bacteriol.* **48,** 179–186
31. Swingley, W. D., Sadekar, S., Mastrian, S. D., Matthies, H. J., Hao, J., Ramos, H., Acharya, C. R., Conrad, A. L., Taylor, H. L., Dejesa, L. C., Shah, M. K., O'huallachain, M. E., Lince, M. T., Blankenship, R. E., Beatty, J. T., and Touchman, J. W. (2007) *J. Bacteriol.* **189,** 683–690
32. Strömpl, C., Hold, G. L., Lünsdorf, H., Graham, J., Gallacher, S., Abraham, W. R., Moore, E. R., and Timmis, K. N. (2003) *Int. J. Syst. Evol. Microbiol.* **53,** 1901–1906
33. Hümbelin, M., Thomas, A., Lin, J., Li, J., Jore, J., and Berry, A. (2002) *Gene* **297,** 129–139
34. Patton, D. E., Isom, L. L., Catterall, W. A., and Goldin, A. L. (1994) *J. Biol. Chem.* **269,** 17649–17655
35. O'Neil, K. T., and DeGrado, W. F. (1990) *Science* **250,** 646–651
36. Lalik, P. H., Krafte, D. S., Volberg, W. A., and Ciccarelli, R. B. (1993) *Am. J. Physiol.* **264,** C803–C809
37. Swartz, T. H., Ikewada, S., Ishikawa, O., Ito, M., and Krulwich, T. A. (2005) *Extremophiles* **9,** 345–354
38. Ito, M., Hicks, D. B., Henkin, T. M., Guffanti, A. A., Powers, B. D., Zvi, L., Uematsu, K., and Krulwich, T. A. (2004) *Mol. Microbiol.* **53,** 1035–1049
39. McEvoy, M. M., and Dahlquist, F. W. (1997) *Curr. Opin. Struct. Biol.* **7,** 793–797
40. Shimizu, H., Iwamoto, M., Konno, T., Nihei, A., Sasaki, Y. C., and Oiki, S. (2008) *Cell* **132,** 67–78
41. Blunck, R., Cordero-Morales, J. F., Cuello, L. G., Perozo, E., and Bezanilla, F. (2006) *J. Gen. Physiol.* **128,** 569–581

J|A|C|S COMMUNICATIONS

Published on Web 03/18/2009

Covalent Protein Labeling Based on Noncatalytic β-Lactamase and a Designed FRET Substrate

Shin Mizukami, Shuji Watanabe, Yuichiro Hori, and Kazuya Kikuchi*

Graduate School of Engineering, Osaka University, 2-1 Yamadaoka, Suita, Osaka 565-0871, Japan

Received October 20, 2008; E-mail: kkikuchi@mls.eng.osaka-u.ac.jp

Fluorescence microscopy is one of the most common techniques employed in the field of life science. With the rapid progress that has been achieved with regard to optical systems, fluorescent proteins (FPs) have acquired important roles for fluorescence microscopy experiments. In order to visualize the localization and behavior of particular proteins of interest, FPs such as green fluorescent protein (GFP) have conventionally been used.[1] More recently, techniques for labeling proteins with small molecules have attracted the attention of many life scientists because they can extend the range of natural FPs, for example, by incorporating near-infrared fluorescent dyes, MRI contrast agents, or biofunctional molecules such as biotin. Several approaches for modifying proteins with small molecules have been commercialized, including methods based on the tetracysteine tag,[2] HaloTag,[3] and SNAP-tag.[4] Other protein labeling methods involving the use of biotin ligase,[5] transglutaminase,[6] hexahistidine,[7] tetra-aspartic acid,[8] etc. have also been reported. Among the abovementioned labeling methods, only the tetracysteine tag exhibits fluorogenic properties. In the other labeling methods, it is necessary to wash the treated cells prior to microscopic measurements to eliminate background fluorescence. Thus, new labeling techniques that satisfy the dual criteria of specificity and fluorogenicity are desirable.

In this paper, we report a specific protein labeling system with an off-on fluorescence switch. It involves covalent modification of a genetically engineered hydrolytic enzyme with a rationally designed fluorogenic probe that exploits the principle of fluorescence resonance energy transfer (FRET). Using this system, we can achieve specific and fluorogenic protein labeling under physiological conditions.

First, we designed the tag protein. Plant or bacterial proteins are preferably used to achieve bioorthogonal labeling in mammalian cells. We focused on β-lactamase as the candidate tag because β-lactamases are small bacterial enzymes that hydrolyze antibiotics containing a β-lactam structure and have no endogenous counterpart among eukaryotic cells.[9] β-Lactamase has been widely used as a reporter enzyme for examining gene expression in living mammalian cells.[10] Class A β-lactamases such as the 29 kDa TEM-1[11] have been extensively investigated with regard to their structures, enzyme reaction kinetics, substrate specificity, inhibitors, etc.[12] The reaction of TEM-1 with β-lactams involves acylation and deacylation steps (Scheme 1). In the acylation step, Ser70 attacks the amide bond of the β-lactam ring to form an intermediate acyl-enzyme complex (ES*). In the deacylation step, an activated water molecule hydrolyzes the ester bond of the intermediate to yield the product. Previous studies have shown that Glu166 is essential for the deacylation step[13] and that the E166N mutant of TEM-1 (^{E166N}TEM) accumulates the acyl-enzyme intermediate by markedly slowing deacylation (k_3) relative to acylation (k_2).[14] We hoped to exploit the properties of the ^{E166N}TEM mutant to covalently attach a fluorescent substrate to β-lactamase.

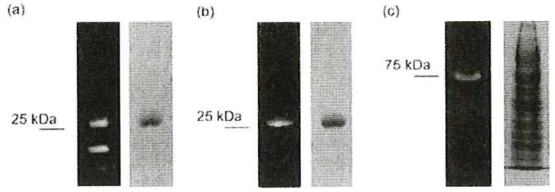

Figure 1. (a, b) Fluorescence (left) and CBB-stained (right) gel images of ^{E166N}TEM after incubation with (a) CA and (b) CCD. (c) Fluorescence and CBB-stained gel image of MBP-^{E166N}TEM mixed with HEK293T cell lysate after incubation with CCD.

Scheme 1. Mechanism of β-Lactam Cleavage by Class A β-Lactamases; (E) Enzyme, (S) Substrate, and (P) Product

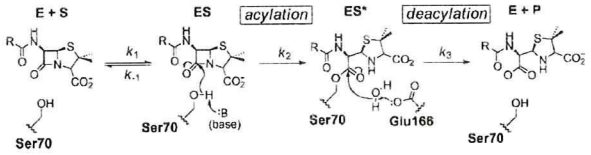

Scheme 2. Structures and Labeling Mechanisms of the Fluorescent Probes (a) CA and (b) CCD

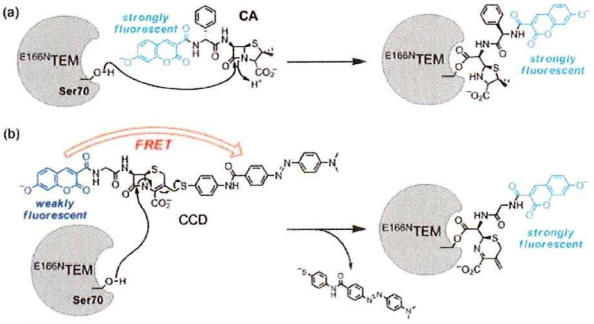

To investigate the feasibility of fluorescently labeling ^{E166N}TEM under physiological conditions, we designed and synthesized a penicillin-based fluorescent probe, coumarinyl ampicillin (CA). The labeling scheme is illustrated in Scheme 2a. Since CA contains 7-hydroxycoumarin, successfully labeled ^{E166N}TEM should exhibit cyan fluorescence. ^{E166N}TEM was incubated with CA in 10 mM Tris-HCl buffer (pH 7.0) at 25 °C, and protein labeling was assessed by SDS-PAGE. Fluorescent proteins were detected by irradiating the gels with UV light at 365 nm. When purified ^{E166N}TEM was mixed with CA, a protein band of ~29 kDa was observed that exhibited cyan fluorescence (Figure 1a); Coomassie Brilliant Blue (CBB) staining confirmed that this band corresponded to ^{E166N}TEM. In contrast, when wild-type (WT) TEM-1 was incubated with CA, no cyan fluorescence was seen (Figure S1a). Although CA successfully labels ^{E166N}TEM, other fluorescent bands were also observed on the gel. Since these bands were also seen when only

10.1021/ja8082285 CCC: $40.75

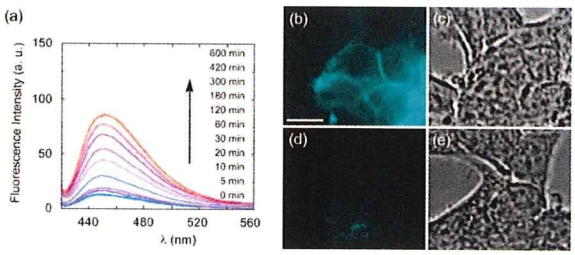

Figure 2. (a) Time-dependent emission spectra (λ_{ex} = 410 nm) of CCD (1 μM) in the presence of ^{E166N}TEM in 100 mM HEPES buffer (pH 7.4) containing 0.1% DMSO at 25 °C. (b−e) Optical microscopic images of CCD-labeled HEK293T cells expressing ^{E166N}TEM-EGFR (b,c) and EGFR (d,e), labeled with 5 μM CCD. (b,d) Fluorescence microscopic images, excitation at 410 nm. (c,e) phase contrast microscopic images. Scale bar: 10 μm.

CA was electrophoresed (Figure S2), a washing procedure should be performed before observation under a fluorescence microscope.

Next, we designed and synthesized CCD (Scheme 2b), a fluorescence off−on labeling probe. This molecule has three main components: 7-hydroxycoumarin, cephalosporin, and 4-(4′-dimethylaminophenylazo)benzoic acid (DABCYL). Since the absorption spectrum of DABCYL substantially overlaps with the emission spectrum of 7-hydroxycoumarin, the fluorescence of CCD would be expected to be largely quenched by intramolecular FRET from coumarin to DABCYL. Based on related probes of β-lactamase activity,[10] cleavage of the β-lactam of CCD by ^{E166N}TEM should result in covalent attachment of the coumarin to the protein with concomitant release of the DABCYL moiety as shown in Scheme 2b. After loss of the DABCYL group, the cyan fluorescence of coumarin should be restored by cancelation of FRET.

The fluorescence spectrum of CCD confirmed that the coumarin fluorescence was almost completely quenched because of FRET. The fluorescence quantum yield of CCD was 0.006, which is much lower than that of CA (Φ = 0.40). When CCD was incubated with ^{E166N}TEM, the fluorescence increased considerably in a time-dependent manner (Figure 2a). This indicates that ^{E166N}TEM cleaved the β-lactam of CCD and eliminated the DABCYL group. When the DABCYL group was completely eliminated by WT TEM-1, the fluorescence signal increased approximately 30-fold. The apparent rate of reaction between CCD and ^{E166N}TEM was approximately 80-fold slower than that of the reaction between CCD and WT TEM-1 (Figure S3), probably because the mutation at E166 decreases the acylation rate (k_2) somewhat.[15]

CCD specifically labels ^{E166N}TEM, as demonstrated by incubation of the probe molecule with both ^{E166N}TEM and WT TEM-1 in 10 mM Tris-HCl buffer (pH 7.0) at 25 °C, followed by SDS-PAGE analysis. As shown in Figure 1b, only the band corresponding to ^{E166N}TEM exhibited cyan fluorescence; no fluorescence was associated with WT TEM-1 (Figure S1b). In contrast to CA, unreacted CCD yielded considerably weaker fluorescence on the gel. In MALDI-TOF MS analyses of the samples, the molecular mass peak for the protein−probe adduct was only detected when ^{E166N}TEM was incubated with CCD (Figure S4).

This system can therefore be used to label target proteins in a biological medium. For example, we fused ^{E166N}TEM to maltose binding protein (MBP, 42 kDa), mixed the purified MBP−^{E166N}TEM construct with HEK293T cell lysate, and incubated the mixture with CCD at 25 °C for 45 min. SDS-PAGE analysis revealed that fusion protein was efficiently and selectively labeled with the fluorogenic probe (Figure 1c).

Finally, we investigated specific labeling of target proteins displayed on the surface of living cells. ^{E166N}TEM was fused to the N-terminus of epidermal growth factor receptor (EGFR), a membrane associated protein, and the construct was produced in HEK293T cells. After treatment with CCD (see Supporting Information), the cells were examined under a fluorescence microscope. Only cells producing the ^{E166N}TEM-EGFR fusion protein emitted cyan fluorescence as a consequence of specific labeling by the probe (Figure 2b−e).

In conclusion, we have developed a novel protein labeling system that combines a genetically modified β-lactamase with low molecular weight fluorogenic β-lactam probes. Through appropriate probe design, we succeeded in labeling proteins with a sensitive fluorophore in vitro and on living cells. In principle, this system does not require washing procedures to remove the unreacted probes after labeling. Furthermore, since the ^{E166N}TEM tag protein is absent in mammalian cells, it can be used for the specific labeling of proteins in higher eukaryotes. We anticipate that this labeling system will find wide application in the field of life science.

Acknowledgment. We thank Dr. Shahriar Mobashery at the University of Notre Dame for kindly providing TEM-1 plasmid. We also thank Dr. Robert E. Campbell at Alberta University, Dr. Gregor Zlokarnik at Vertex Pharmaceuticals, and Dr. Donald Hivert at ETH Zürich for helpful discussions. S.W. acknowledges a Global COE Fellowship of Osaka University. This work was supported in part by MEXT of Japan.

Supporting Information Available: Detailed experimental procedures and supplementary figures. This material is available free of charge via the Internet at http://pubs.acs.org.

References

(1) Chudakov, D. M.; Lukyanov, S.; Lukyanov, K. A. *Trends Biotechnol.* **2005**, *23*, 605–613.
(2) Griffin, B. A.; Adams, S. R.; Tsien, R. Y. *Science* **1998**, *281*, 269–272.
(3) Los, G. V.; et al. *ACS Chem. Biol.* **2008**, *3*, 373–382.
(4) Keppler, A.; Gendreizig, S.; Pick, H.; Vogel, H.; Johnsson, K. *Nat. Biotechnol.* **2003**, *21*, 86–89.
(5) Chen, I.; Howarth, M.; Lin, W.; Ting, A. Y. *Nat. Methods* **2005**, *2*, 99–104.
(6) Lin, C.-W.; Ting, A. Y. *J. Am. Chem. Soc.* **2006**, *128*, 4542–4543.
(7) Hauser, C. T.; Tsien, R. Y. *Proc. Natl. Acad. Sci. U.S.A.* **2007**, *104*, 3693–3697.
(8) Ojida, A.; Honda, K.; Shinmi, D.; Kiyonaka, S.; Mori, Y.; Hamachi, I. *J. Am. Chem. Soc.* **2006**, *128*, 10452–10459.
(9) Waley, S. G. *In the chemistry of β-lactams*; Page, M. I., Ed.; Chapman & Hall: London, 1992; p 198.
(10) (a) Moore, J. T.; Davis, S. T.; Dev, I. K. *Anal. Biochem.* **1997**, *247*, 203–209. (b) Zlokarnik, G.; Negulescu, P. A.; Knapp, T. E.; Mere, L.; Burres, N.; Feng, L.; Whitney, M.; Roemer, K.; Tsien, R. Y. *Science* **1998**, *279*, 84–88. (c) Gao, W.; Xing, B.; Tsien, R. Y.; Rao, J. *J. Am. Chem. Soc.* **2003**, *125*, 11146–11147. (d) Campbell, R. E. *Trends Biotechnol.* **2004**, *22*, 208–211. (e) Xing, B.; Khanamiryan, A.; Rao, J. *J. Am. Chem. Soc.* **2005**, *127*, 4158–4159.
(11) Sutcliffe, J. G. *Proc. Natl. Acad. Sci. U.S.A.* **1978**, *75*, 3737–3741.
(12) Matagne, A.; Lamotte-Blasseur, J.; Frére, J.-M. *Biochem. J.* **1998**, *330*, 581–598.
(13) Guillaume, G.; Vanhove, M.; Lamotte-Brasseur, J.; Ledent, P.; Jamin, M.; Joris, B.; Frére, J.-M. *J. Biol. Chem.* **1997**, *272*, 5438–5444.
(14) Adachi, H.; Ohta, T.; Matsuzawa, H. *J. Biol. Chem.* **1991**, *266*, 3186–3191.
(15) Vijayakumar, S.; Ravishanker, G.; Pratt, R. F.; Beveridge, D. L. *J. Am. Chem. Soc.* **1995**, *117*, 1722–1730.

JA8082285

DOI: 10.1002/anie.200806328

Molecular Imaging

Dual-Function Probe to Detect Protease Activity for Fluorescence Measurement and ^{19}F MRI**

*Shin Mizukami, Rika Takikawa, Fuminori Sugihara, Masahiro Shirakawa, and Kazuya Kikuchi**

Noninvasive molecular imaging techniques are important for understanding the actual mechanisms of biological systems. In biological sciences, especially those involving cellular systems, the most widely used imaging technique is fluorescence microscopy, because of its high sensitivity, high spatiotemporal resolution, and simple experimental procedure.[1] On the other hand, magnetic resonance imaging (MRI) is one of the most successful imaging techniques in the field of clinical diagnosis. As MRI can visualize deep regions of animal bodies,[2] application of MRI to in vivo imaging of biomolecules is attracting attention.[3] Several ^{1}H MRI probes have been developed to investigate pH values,[4] metal ions,[5] and enzyme activities.[6]

Recently, heteronuclear MRI has been attracting considerable attention as an alternative molecular imaging technique. One of the most promising nuclides for MRI is ^{19}F,[7] which has a high NMR sensitivity that is comparable to that of ^{1}H, and almost no intrinsic ^{19}F signals can be observed in living animals. ^{19}F MRI does not have the drawback of background signals from intrinsic biomolecules, which interfere with the probe signals. Very recently, we developed a novel design strategy for ^{19}F MRI probes that can detect protease activity.[8] We exploited the paramagnetic relaxation enhancement (PRE) effect to achieve off/on switching of the probe MRI signals (Scheme 1 a). Using the ^{19}F MRI probe Gd-DOTA-DEVD-Tfb (Tfb = *para*-trifluoromethoxybenzyl) based on this mechanism, we were successful in detecting caspase-3 activity by ^{19}F MRI.

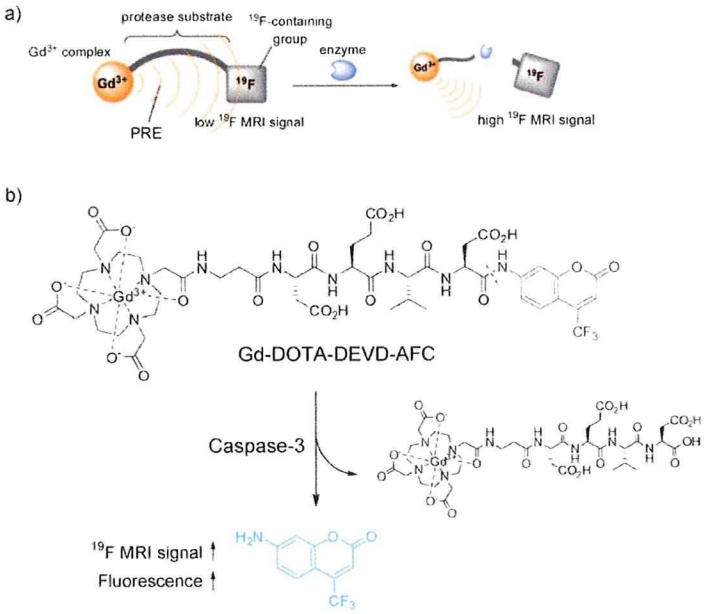

Scheme 1. a) Representation of ^{19}F MRI detection of protease activity. b) Chemical structure of Gd-DOTA-DEVD-AFC and its reaction scheme for detecting caspase-3 activity.

Although MRI can visualize deep regions of living bodies, its sensitivity is inferior to that of fluorescence measurement. The lower sensitivity requires longer accumulation time for imaging. If the probes are multifunctional, we can choose the appropriate imaging method in accordance with the experimental conditions. Higuchi et al. developed the dual-function probe (*E*,*E*)-1-fluoro-2,5-bis(3-hydroxycarbonyl-4-hydroxy)-styrylbenzene (FSB), which aggregates to amyloidβ (Aβ) plaques, for ^{19}F MRI and fluorescence measurements.[9] ^{19}F MRI signals localized on Aβ plaques were observed in living mice in vivo, and fluorescence signals in brain slices ex vivo.[9] As such complementary experiments have resulted in more reliable conclusions, development of multimodal imaging probes is very important.[10] Herein we report a dual-function probe to detect protease activity by fluorescence measurement and ^{19}F MRI that is based on the development of Gd-DOTA-DEVD-Tfb.[8]

We chose 7-amino-4-trifluoromethylcoumarin (AFC) as a reporter group that is active in both ^{19}F MRI and fluorescence measurement. AFC is strongly fluorescent in polar solvents,

[*] Dr. S. Mizukami, R. Takikawa, Prof. K. Kikuchi
Graduate School of Engineering
Osaka University, Osaka 565-0871 (Japan)
Fax: (+81) 6-6879-7924
E-mail: kkikuchi@mls.eng.osaka-u.ac.jp
Homepage: http://www-molpro.mls.eng.osaka-u.ac.jp/
F. Sugihara
International Graduate School of Arts and Sciences
Yokohama City University, Kanagawa 230-0045 (Japan)
Cellular & Molecular Biology Laboratory
RIKEN Advanced Science Institute
Saitama 351-0198 (Japan)
Prof. M. Shirakawa
Graduate School of Engineering
Kyoto University, Kyoto 615-8510 (Japan)
CREST, Science and Technology Corporation, Saitama 332-0012 (Japan)

[**] This work was supported in part by MEXT of Japan. MRI = magnetic resonance imaging.

Supporting information for this article is available on the WWW under http://dx.doi.org/10.1002/anie.200806328.

and the fluorescence properties of 7-aminocoumarin derivatives depend on the electron-donating ability of the 7-amino group.[11] Usually, the peptide modification on the 7-amino group induces a blue shift of the fluorescence spectrum with a decrease in fluorescence intensity. Thus, AFC has been utilized as the fluorophore for protease activity detection.[12] Furthermore, the ^{19}F NMR spectrum of AFC shows only a singlet peak without any coupling to intramolecular protons. AFC is thus appropriate for ^{19}F MRI.

We designed a bimodal probe Gd-DOTA-DEVD-AFC (Scheme 1), in which the probe consists of mainly three parts: Gd^{3+}-DOTA complex (DOTA = 1,4,7,10- tetraazacyclododecane-1,4,7,10-tetraacetate), caspase-3 substrate peptide (DEVD), and ^{19}F-containing fluorophore (AFC). When caspase-3 cleaves the C terminus of the DEVD sequence, AFC is produced. After the enzyme is cleaved, the ^{19}F MRI signal is increased in much the same manner as in Gd-DOTA-DEVD-Tfb (Scheme 1 a). Simultaneously, the fluorescence spectrum of AFC is increased. Thus, Gd-DOTA-DEVD-AFC is expected to work as a bimodal probe that detects caspase-3 activity.

The Gd-DOTA-DEVD-AFC probe was synthesized using Fmoc solid-phase chemistry, followed by complex formation with the Gd^{3+} ion (Scheme 2). The excitation peak of Gd-DOTA-DEVD-AFC is at 340 nm, and irradiation at 400 nm results in little fluorescence emission. The incubation of the probe with caspase-3 at 37 °C induced the excitation spectral shift toward longer wavelengths. Therefore, when the probe was excited at 400 nm, the emission at around 500 nm was substantially increased (Figure 1). From the fluorescence measurements, the kinetic parameters for hydrolysis of Gd-DOTA-DEVD-AFC by caspase-3 were measured. The V_{max}/K_m value of Gd-DOTA-DEVD-AFC is 7.61×10^{-3} s^{-1}. On the other hand, V_{max}/K_m of Ac-DEVD-AMC, the commercially available fluorescent substrate (AMC = 7-amino-4-methylcoumarin), is 9.91×10^{-4} s^{-1}. This result indicates that Gd-DOTA complex does not hinder the enzyme reaction at all. Thus, Gd-DOTA-DEVD-AFC can be used as a superior fluorogenic probe for detecting caspase-3 activity.

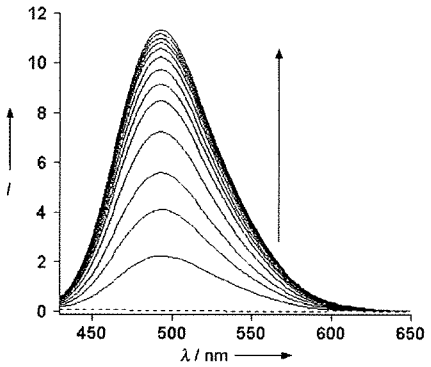

Figure 1. Time-dependent emission spectra of Gd-DOTA-DEVD-AFC (10 μM) with casapse-3 (0.84 mU) in the reaction buffer (pH 7.4) at 37 °C. The spectra were measured every 2 min after the addition of the enzyme. The dotted line indicates no caspase-3. The excitation wavelength: 400 nm. Reaction buffer: 4-(2-hydroxyethyl)-1-piperazineethanesulfonic acid (HEPES, pH 7.4, 50 mM) containing glycerol (10%), NaCl (100 mM), dithiothritol (DTT, 10 mM), ethylenediaminetetraacetic acid (EDTA, 1 mM), and 3-[(3-cholamidopropyl)dimethylammonio]-1-propanesulfonate (CHAPS, 0.1%).

We measured the ^{19}F NMR spectra of Gd-DOTA-DEVD-AFC and its metal-free analogue DOTA-DEVD-AFC. The NMR signal of Gd-DOTA-DEVD-AFC was broad and weak compared to that of the Gd^{3+}-free DOTA-DEVD-AFC (Supporting Information). This change in peak shape and intensity suggests that ^{19}F undergoes an intramolecular PRE effect from the Gd^{3+} ion. Longitudinal (T_1) and transverse (T_2) relaxation times of DOTA-DEVD-AFC (250 μM) were (0.479 ± 0.003) s and (0.152 ± 0.006) s, respectively (Table 1). In case of Gd-DOTA-DEVD-AFC, we could not estimate either T_1 or T_2, because these relaxation times were markedly shorter and the ^{19}F NMR signal intensity was low. From molecular modeling, the distance between the Gd^{3+} ion and the ^{19}F atom in the probe was estimated to be less than 25 Å. However, as the substrate peptide is flexible, the Gd^{3+} ion can be distributed in closer proximity to ^{19}F, such that the PRE effect works efficiently.

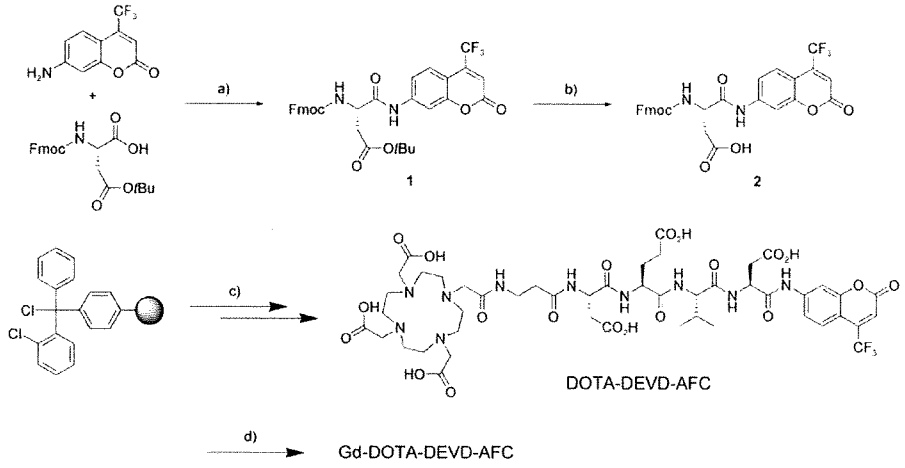

Scheme 2. Synthetic route to Gd-DOTA-DEVD-AFC. a) $POCl_3$, pyridine. b) trifluoroacetic acid. c) Fmoc peptide synthesis: **2**, Fmoc-Val-OH, Fmoc-Glu(O*t*Bu)-OH, Fmoc-Asp(O*t*Bu)-OH, Fmoc-β-Ala-OH, tris-*t*Bu-DOTA, deprotection. d) $GdCl_3 \cdot 6H_2O$, 100 mM HEPES buffer (pH 7.4). Fmoc = fluorenylmethyloxycarbonyl.

Next, we performed an enzyme assay using ^{19}F NMR spectroscopy. When Gd-DOTA-DEVD-AFC was treated with caspase-3 in the reaction buffer at 37 °C, a sharper and a more intense ^{19}F NMR signal was observed, with a slight downfield shift (Figure 2). T_1 and T_2 of the cleaved product (250 μM) were elongated to (0.38 ± 0.04) s and (0.097 ± 0.004) s, respectively (Table 1). This finding indicates that the intramolecular PRE effect from the Gd^{3+} ion to the ^{19}F atom was cancelled owing to the cleavage of the probe. After complete cleavage by

Table 1: Longitudinal and transverse relaxation times of synthesized probes.

	T_1 [s][a]	T_2 [s][a]
DOTA-DEVD-AFC	0.479(3)	0.152(6)
Gd-DOTA-DEVD-AFC	–[b]	–[b]
Gd-DOTA-DEVD-AFC + caspase-3	0.38(4)[c]	0.097(4)[c]

[a] Parenthesis denotes standard deviation ($n=3$). [b] The relaxation time was too short to be determined. [c] The relaxation times were measured after the enzyme (250 μM) reaction was complete.

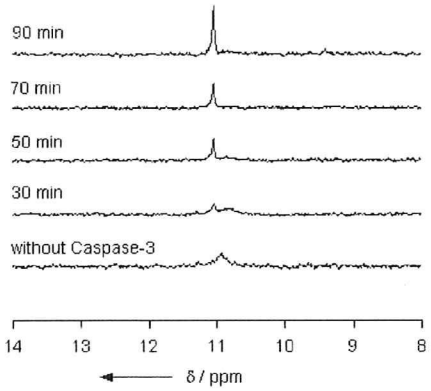

Figure 2. Time-dependent ^{19}F NMR spectra of Gd-DOTA-DEVD-AFC (250 μM) after addition of caspase-3 (1.25 mU) at 37 °C. Reaction buffer: As in Figure 1 plus D_2O (5%).

caspase-3 (confirmed by HPLC), the relaxation times T_1 and T_2 were lower than those observed for the metal-free ligand. These shorter relaxation times are most likely due to the intermolecular PRE of the cleaved Gd-DOTA (Supporting Information, Figure S4).

Finally, we attempted to visualize caspase-3 activity using a ^{19}F MRI phantom with Gd-DOTA-DEVD-AFC. Because of the extremely short relaxation time T_2, the ^{19}F MRI of Gd-DOTA-DEVD-AFC had no signals. When caspase-3 was added to the solution of Gd-DOTA-DEVD-AFC, augmentation of the ^{19}F MRI signal of the probe was observed (Figure 3).

In conclusion, we developed a novel dual-function probe, Gd-DOTA-DEVD-AFC, which detects caspase-3 activity by dual signal increase in fluorescence and in ^{19}F MRI. Because fluorescence measurement and MRI provide complementary information, such dual-mode probes should be quite useful for various biological experiments. Although several multimodal probes, such as fluorescence measurement and MRI, have been developed recently,[13] most probes are constructed by simple attachment of reporter moieties such as fluorescence dyes or MRI contrast agents. In contrast, multimodal probes accompanying plural signal enhancement have been scarcely reported. Such multimodal smart probes would be the next-generation probes in multimodal imaging for detecting enzyme activity.

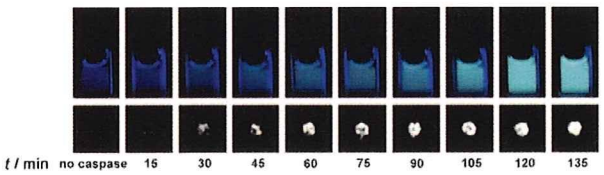

Figure 3. Time-dependent fluorescence images (top, λ_{ex}: 400 nm) and ^{19}F MR phantom images (bottom, diameter: approximately 2 mm) of Gd-DOTA-DEVD-AFC (10 μM for fluorescence measurement and 1 mM for ^{19}F MRI) with caspase-3 (60 nU for fluorescence measurement and 2 mU for ^{19}F MRI) at 37 °C. Reaction buffer: As in Figure 1. For ^{19}F MRI, [D_6]DMSO (20%) was introduced into the reaction buffer.

Received: December 26, 2008
Published online: April 7, 2009

Keywords: fluorescence · magnetic resonance imaging · molecular imaging · multimodal probe · proteases

[1] J. R. Lakovicz, *Principles of Fluorescence Spectroscopy*, 3rd ed., Springer Science & Business Media, New York, **2006**.
[2] a) A. Jasanoff, *Trends Neurosci.* **2005**, *28*, 120–126; b) D. E. Sosnovik, R. Weissleder, *Curr. Opin. Biotechnol.* **2007**, *18*, 4–10.
[3] R. Weissleder, M. J. Pittet, *Nature* **2008**, *452*, 580–589.
[4] a) S. Zhang, W. Kuangcong, A. D. Sherry, *Angew. Chem.* **1999**, *111*, 3382–3384; *Angew. Chem. Int. Ed.* **1999**, *38*, 3192–3194; b) S. Aime, A. Barge, D. D. Castelli, F. Fedeli, A. Mortillaro, F. U. Nielsen, E. Terreno, *Magn. Reson. Med.* **2002**, *47*, 639–648.
[5] a) W. Li, S. E. Fraser, T. J. Meade, *J. Am. Chem. Soc.* **1999**, *121*, 1413–1414; b) K. Hanaoka, K. Kikuchi, Y. Urano, M. Narazaki, T. Yokawa, S. Sakamoto, K. Yamaguchi, T. Nagano, *Chem. Biol.* **2002**, *9*, 1027–1032.
[6] a) A. Y. Louie, M. M. Hüber, E. T. Ahrens, U. Rothbächer, R. Moats, R. E. Jacobs, S. E. Fraser, T. J. Meade, *Nat. Biotechnol.* **2000**, *18*, 321–325; b) J. M. Perez, L. Josephson, T. O'Loughlin, D. Högemann, R. Weissleder, *Nat. Biotechnol.* **2002**, *20*, 816–820; c) B. Yoo, M. D. Pagel, *J. Am. Chem. Soc.* **2006**, *128*, 14032–14033; d) J. W. Chen, M. Q. Sans, A. Bogdanov, R. Weissleder, *Radiology* **2006**, *240*, 473–481.
[7] J. Yu, V. D. Kodibagkar, W. Cui, R. P. Mason, *Curr. Med. Chem.* **2005**, *12*, 819–848.
[8] S. Mizukami, R. Takikawa, F. Sugihara, Y. Hori, H. Tochio, M. Wälchli, M. Shirakawa, K. Kikuchi, *J. Am. Chem. Soc.* **2008**, *130*, 794–795.
[9] M. Higuchi, N. Iwata, Y. Matsuba, K. Sato, K. Sasamoto, T. C. Saido, *Nat. Neurosci.* **2005**, *8*, 527–533.
[10] a) E. A. Schellenberger, D. Sosnovik, R. Weissleder, L. Josephson, *Bioconjugate Chem.* **2004**, *15*, 1062–1067; b) Y. M. Huh, Y. W. Jun, H. T. Song, S. Kim, J. S. Choi, J. H. Lee, S. Yoon, K. S. Kim, J. S. Shin, J. S. Suh, J. Cheon, *J. Am. Chem. Soc.* **2005**, *127*, 12387–12391; c) P. Sharma, S. Brown, G. Walter, S. Santra, B. Moudgil, *Adv. Colloid Interface Sci.* **2006**, *123–126*, 471–485; d) J. H. Choi, F. T. Nguyen, P. W. Barone, D. A. Heller, A. E. Moll, D. Patel, S. A. Boppart, M. S. Strano, *Nano Lett.* **2007**, *7*, 861–867.
[11] C. E. Wheelock, *J. Am. Chem. Soc.* **1959**, *81*, 1348–1352.
[12] R. E. Smith, E. R. Bissel, A. R. Mitchell, K. W. Pearson, *Thromb. Res.* **1980**, *17*, 393–402.
[13] a) Y. M. Huh, Y. W. Jun, H. T. Song, S. Kim, J. S. Choi, J. H. Lee, S. Yoon, K. S. Kim, J. S. Shin, J. S. Suh, J. Cheon, *J. Am. Chem. Soc.* **2005**, *127*, 12387–12391; b) J. H. Lee, Y. W. Jun, S. I. Yeon, J. S. Shin, J. Cheon, *Angew. Chem.* **2006**, *118*, 8340–8342; *Angew. Chem. Int. Ed.* **2006**, *45*, 8160–8162; c) S. A. Corr, Y. P. Rakovich, Y. K. Gun'ko, *Nanoscale Res. Lett.* **2008**, *3*, 87–104; d) K. Tanaka, K. Inafuku, Y. Chujo, *Bioorg. Med. Chem.* **2008**, *16*, 10029–10033.

DOI: 10.1002/cbic.200900214

Development of Ratiometric Fluorescent Probes for Phosphatases by Using a pK_a Switching Mechanism

Shin Mizukami, Shuji Watanabe, and Kazuya Kikuchi*[a]

The use of fluorescent probes in fluorimetric assays is particularly useful in physiological studies because of their high sensitivity and noninvasiveness. For example, the widely used Ca^{2+} probe fura-2[1] and the subsequently developed fluorescent probes[2] have contributed significantly to the rapid progress of intracellular Ca^{2+} signaling studies. One of the outstanding characteristics of fura-2 is that it exhibits a shift in its excitation spectra in response to changes in Ca^{2+} concentration, which enables ratiometric fluorescence measurement at two wavelengths. Ratiometric measurement, in which the fluorescence intensity is monitored at two excitation or two emission wavelengths and the ratio of the two values is calculated, is more practical than normal fluorescence intensity measurement, because ratiometric measurement can exclude such variables as the influence of dye localization and fluctuation of excitation light intensity.[3]

For the rational design of ratiometric fluorescent probes, the resonance energy transfer (RET) mechanism is quite useful.[4] However, small-molecule RET probes generally require complicated synthesis, which involves conjugation of two different fluorescent dyes. Therefore, a new design principle for ratiometric probes is required. In this study, we developed a novel design strategy for ratiometric fluorescent probes. We applied this strategy in the development of fluorescent probes for detecting phosphatase activity.

Phosphatases catalyze the dephosphorylation of various types of biomolecules, including proteins, nucleic acids, and lipids, and play significant roles in the regulation of metabolic pathways in living organisms. Phosphatases are categorized into several groups, including alkaline phosphatases (ALP),[5] acid phosphatases (ACP),[6] serine/threonine phosphatases,[7] and tyrosine phosphatases (PTP)[8] to name a few. Thus far, several fluorescent probes have been developed for detecting phosphatase activity.[9–12] One prototype is 4-methylumbelliferyl phosphate (MUP),[9] which is hydrolyzed by several types of phosphatases, resulting in an increase in the fluorescence intensity. Other fluorescent phosphatase probes such as 3,6-fluorescein diphosphate (FDP)[10] and 6,8-difluoro-4-methylumbelliferyl phosphate (DiFMUP)[11] are also widely used. However, these probes do not have ratiometric fluorescence properties. Thus, the development of ratiometric fluorimetric probes that can detect phosphatase activities has been attempted by many research groups.

In addition to the aforementioned limitation, known phosphatase probes have another drawback: they have an aryl phosphate monoester moiety; phosphodiesterases convert them to the corresponding aryl alcohol, which fluoresce more strongly than the phosphate monoesters. Although they are considered structural analogues of phosphotyrosine and are used as fluorescent probes for detecting tyrosine phosphatase activity,[11,12] they are hydrolyzed by serine/threonine phosphatases[13] and ALP/ACP.[13,14] Usually, several types of phosphatase are activated in biological samples. When known phosphatase probes such as DiFMUP are used for the detection of phosphatase activity, the output fluorescence signal represents the sum of the activities of several phosphatases. Therefore, there is a requirement for more specific probes for individual phosphatases. For developing a specific probe for a phosphatase, the design of the enzyme-recognizing structure is important. The known probes always require an aryl phosphate monoester structure, and this structural requirement imposes severe limitations on probe design. Herein we report a novel design strategy for fluorescent probes that have an alkyl phosphate monoester structure. We investigated the specificity of the synthesized probes toward several phosphatases and discuss the correlation between their structure and the kinetic parameters in reaction with ACP.

In our design of new ratiometric probes, we initially focused on the fluorescence properties of coumarins. Coumarins containing an electron-donating substituent at the 6- or 7-position generally fluoresce in aqueous solution and have been extensively used for the fluorescence detection of various enzyme activities.[9,11,13,15] In particular, 7-hydroxycoumarins (umbelliferones) have been widely used because they have strong fluorescence intensities and they are easily synthesized. One of their distinctive characteristics is that their fluorescence properties are affected by solution pH;[16] excitation wavelength maxima (λ_{ex}) are approximately 330 and 370 nm in acidic and alkaline solution, respectively (Figure 1A). This is because the protonation of the 7-hydroxy group affects fluorescence. By varying the pK_a value of the 7-hydroxy group through judicious substitution, the relative proportion of the phenol and phenolate forms in a neutral buffered solution can be systematically varied. Thus, if the pK_a value of the 7-hydroxy group can be controlled by an enzymatic reaction, the excitation spectrum of coumarin would change in response to the enzyme activity.

The conventional approach to vary the pK_a values of 7-hydroxycoumarins involves substitution of the hydrogen atom at the 6- or 8-position with a halogen atom such as fluorine or chlorine; this substitution decreases the pK_a value by an induc-

[a] Dr. S. Mizukami, S. Watanabe, Prof. K. Kikuchi
Division of Advanced Science and Biotechnology
Graduate School of Engineering, Osaka University
2-1 Yamadaoka, Suita, Osaka, 565-0871 (Japan)
Fax: (+81) 6-6879-7924
E-mail: kkikuchi@mls.eng.osaka-u.ac.jp

Supporting information for this article is available on the WWW under http://dx.doi.org/10.1002/cbic.200900214.

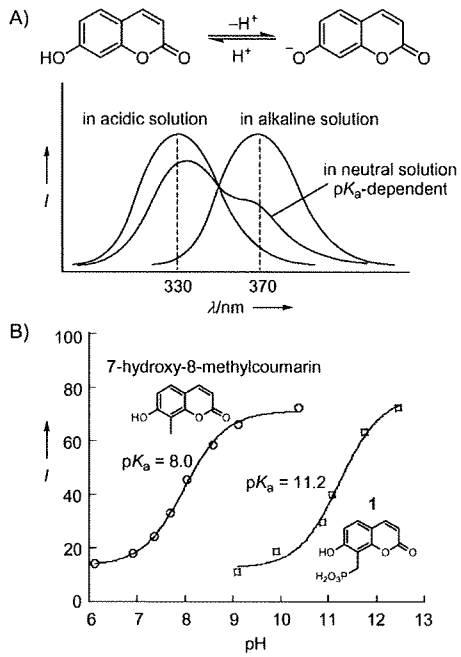

Figure 1. A) pH dependence of the excitation spectra of 7-hydroxycoumarin in aqueous solution (I = fluorescence intensity). B) Effect of a neighboring anionic group on the pK_a values of 7-hydroxycoumarins; fluorescence intensities were measured at λ_{ex} = 380 nm and λ_{em} = 470 nm (25 °C).

tive effect.[17] On the other hand, it has been reported that Calcein Blue (pK_a = 6.9[18]) and other 8-aminomethyl-substituted 7-hydroxycoumarins (pK_a = 6.6–6.7[19]) have lower pK_a values than 7-hydroxy-4-methylcoumarin (pK_a = 7.8[17]). In these cases, the positively charged ammonium groups probably interact with the 7-hydroxy group through hydrogen bonding or electrostatic interactions to enhance deprotonation. By extending this concept, we hypothesized that an anionic group at the 6- or 8-position might increase the pK_a value of the 7-hydroxy group in the opposite manner.

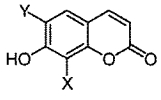

Compound	X	Y
1	$CH_2PO_3H_2$	H
2	$CH_2OPO_3H_2$	H
3a	$CH_2CH_2OPO_3H_2$	H
3b	CH_2CH_2OH	H
4a	H	$CH_2CH_2OPO_3H_2$
4b	H	CH_2CH_2OH
5a	$CH_2CH_2CH_2OPO_3H_2$	H
5b	$CH_2CH_2CH_2OH$	H

To confirm our hypothesis, we synthesized 7-hydroxy-8-phosphorylmethylcoumarin **1** (the synthesis is shown in Scheme S1 in the Supporting Information) and estimated the pK_a value from the fluorescence intensity at various pH values (Figure 1B). As expected, the pK_a value of **1** was considerably higher (pK_a = 11.2) than that of 7-hydroxy-8-methylcoumarin (pK_a = 8.0). This indicates a strong interaction between the anionic phosphate group and the 7-hydroxy group. We exploited this pK_a switch to develop a new type of fluorescent probe, as shown in Figure 2. Here, an anionic group is introduced in the coumarin scaffold at the 6- or 8-position through a tether to increase the pK_a value of the 7-hydroxy group.

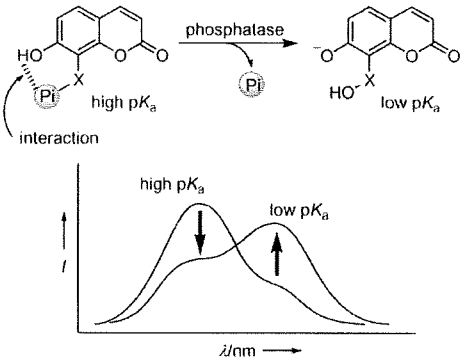

Figure 2. Change in the excitation spectrum of 7-hydroxycoumarin derivatives upon reaction with phosphatases (Pi: phosphate group, X: alkyl linker).

After enzymatic removal of this moiety, the pK_a value would decrease due to loss of the electrostatic interaction, resulting in a change in the excitation spectrum. We selected a phosphate group as the leaving anionic group. In this case, the probe can detect phosphatase activities.

We synthesized 7-hydroxy-8-phosphoryloxymethylcoumarin **2**. However, the compound was unstable and decomposed in aqueous solution. This is probably because the 7-hydroxy group accelerated the removal of the phosphate group to form quinone methide, as reported previously,[16] as phosphate is a good leaving group. We then synthesized **3a**, which has an 8-phosphoryloxyethyl group. We also synthesized **4a** and **5a** in order to examine the effect of the position of the anionic group and the alkyl chain length, respectively. Compounds **3b**–**5b**, lacking phosphate, were synthesized as control compounds. The synthetic routes are shown in Scheme S2 in the Supporting Information.

The pH dependence of the excitation spectrum of **3a** was measured (Figure 3A). Peaks were observed at 333 nm (pH 4.5) and 381 nm (pH 9.3). Between pH 6.5 and 9.3, the excitation spectrum has an isosbestic point at 350 nm; this indicates that only two species, the protonated and deprotonated forms of the 7-hydroxy group, are present in this pH range. The pK_a values of the 7-hydroxy groups of **3a** and **3b** were calculated to be 8.3 and 7.8, respectively, by curve fitting from plots of fluorescence intensity (λ_{ex} = 380 nm, λ_{em} = 470 nm) versus pH (Figure 3B). As we had hypothesized, **3a** showed a greater pK_a value than **3b**.

Compounds **4a** and **5a** showed similar pK_a values (8.1 and 8.2, respectively). The pK_a values of the corresponding dephosphorylated products **4b** and **5b** were 7.7 and 7.8, respectively. In each case, the pK_a value of the phosphate monoester is greater than that of the corresponding alcohol. On the basis of

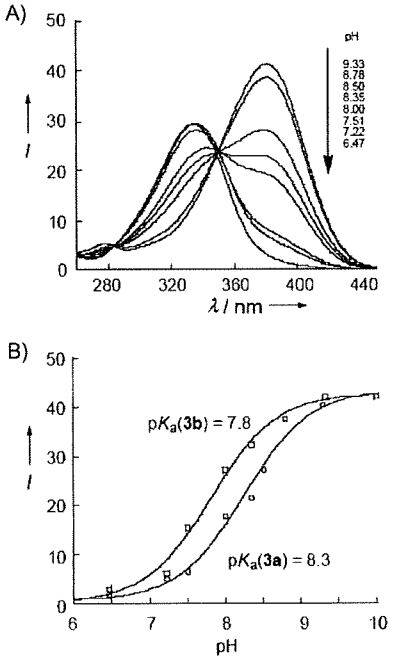

Figure 3. A) Change in the excitation spectrum of **3a** at various pH values (λ_{em} = 470 nm). B) Fluorescence intensities of **3a** (○) and **3b** (□) at various pH values (λ_{ex} = 380 nm, λ_{em} = 470 nm).

these results, it was expected that the excitation spectrum of **3a**–**5a** in neutral buffer solution would change after phosphatase-mediated dephosphorylation, as shown in Figure 2.

We examined the suitability of these compounds as fluorescence probes for phosphatases. When ACP was added to a 10 μM solution of **3a**, the excitation spectrum changed in the expected manner as a function of time. Compounds **4a** and **5a** showed similar spectral changes. For example, the excitation spectrum of **5a** shows a decrease at 330 nm and an increase at 380 nm (Figure 4), originating from the protonated and the deprotonated forms, respectively. The occurrence of the enzyme reaction was confirmed by HPLC (Figure S1, Supporting Information).

Next, we studied the reactivity of other phosphatases toward **3a**. As expected, **3a** was not dephosphorylated by

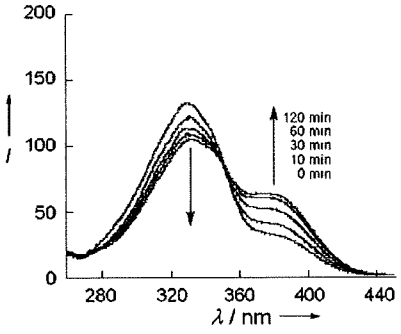

Figure 4. Excitation spectra of **5a** before and after the addition of ACP in 100 mM HEPES buffer solution (pH 7.4) (λ_{em} = 470 nm).

PTPs (CD45 and PTP1B) or by serine/threonine phosphatases (PP1 and $PP2A_1$). On the other hand, ALP induced a partial change in the excitation spectrum of **3a**. However, the reaction rate decreased progressively as the reaction proceeded. This result suggests that the reaction product **3b** inhibits ALP activity. To confirm this putative product inhibition, we examined the effect of **3b** on the fluorescence intensity increase of a commercial fluorescent substrate, DiFMUP. The fluorescence intensity of DiFMUP increased significantly after the addition of ALP, whereas pre-incubation with **3b** inhibited this increase (Figure S2, Supporting Information). This supports the view that **3b** causes product inhibition. This inhibition was not observed with the other phosphatases we studied, so this may provide a clue to the development of selective ALP inhibitors. It is also noteworthy that some coumarin derivatives are protein kinase inhibitors.[17]

To examine the properties of the new fluorescent probes more quantitatively, we estimated the parameters K_M and V_{max} of ACP for **3a**–**5a** by fitting the plot of the initial velocity of the enzyme reaction versus substrate concentration with the Michaelis–Menten equation (Table 1). DiFMUP was used as the

Table 1. Kinetic parameters of **3a**, **4a**, and **5a** with acid phosphatase.[a]

Compound	K_M [μM]	$V_{max} \times 10^9$ [M min^{-1}]	V_{max}/K_M [min^{-1}]
3a	54 ± 18	4.7 ± 0.3	8.7×10^{-5}
4a	107 ± 27	53 ± 3	5.0×10^{-4}
5a	32 ± 12	17 ± 2	5.3×10^{-4}
DiFMUP	41 ± 19	31 ± 9	7.6×10^{-4}

[a] Kinetic data were measured at 30 °C in 100 mM HEPES buffer (pH 7.4) containing 1.0 mM DTT and 1.0 mM EDTA.

standard substrate under the same conditions. Among the three synthesized probes, **4a** and **5a** showed high V_{max}/K_M values, which were similar to that of DiFMUP, whereas **3a** was the worst substrate. The difference in the V_{max}/K_M values of **3a** and **4a** presumably reflects the difference in steric crowding around the phosphate group, because **3a** and **4a** are regioisomers; that is, **3a** is an 8-substituted coumarin and **4a** is a 6-substituted coumarin, and the 6-position of 7-hydroxycoumarin is less crowded than the 8-position. Compound **5a** had an additional methylene group in the linker, and it showed an approximate sixfold increase in the V_{max}/K_M value in comparison with **3a**. This finding indicates that further modification of the linker group might yield more selective and reactive fluorescent probes for ACP. Our design principle could also be used to develop specific probes not only for ACP but for other phosphatases as well.

In conclusion, we have developed a novel design strategy using a pK_a switching mechanism for the design of ratiometric fluorescent probes to detect phosphatase activity. This design strategy is based on a pK_a shift of the 7-hydroxy group of 7-hydroxycoumarin derivatives induced by an adjacent anionic group, which is directly coupled to a change in the excitation spectrum. The synthesized probes are efficiently dephosphorylated by ACP, and changes in the excitation spectrum are ob-

served. These probes are not dephosphorylated by two protein tyrosine phosphatases (PTP1B and CD45) and serine/threonine phosphatases (PP1 and $PP2A_1$), but are slightly dephosphorylated by ALP. The widely used fluorescent phosphatase probe, DiFMUP, responds to all types of phosphatase activity; therefore, our new probes show different enzyme specificity from previously known probes. The enzyme kinetic data indicate that modification of the linker could dramatically change the enzyme affinity.

Our probe design strategy has afforded ACP-selective fluorescent probes. However, in principle, the probe structure can be changed significantly, provided that the hydroxy group (the 7-hydroxy group in this case) interacts with the ionic group (phosphate group in this case). Thus, this strategy should be applicable to the synthesis of fluorescent probes that are highly specific for various types of phosphatases by modifying the linker structure. Further, as discussed above, ratiometric fluorescent probes are preferable for quantitative bio-imaging experiments. As our probe design strategy intrinsically yields ratiometric probes, it should be helpful for the rational development of a wide range of fluorescent probes for the ratiometric bio-imaging of various hydrolases such as phosphodiesterases and sulfatase in living organisms.

Acknowledgements

This work was supported by MEXT of Japan (Grants 18310144 to K.K. and 19710185 to S.M.), the Special Coordination Funds for the Council of Science and Technology Policy (MEXT and JST), the Mitsubishi Foundation, the Shimadzu Science Foundation, the Kato Memorial Bioscience Foundation, the Astellas Foundation for Research on Metabolic Disorders, the Uehara Memorial Foundation, the Terumo Life Science Foundation, the Nagase Science and Technology Foundation, the Asahi Glass Foundation (to K.K.), and the Cosmetology Research Foundation (to S.M.). S.W. expresses his special thanks for The Global COE Program of Osaka University.

Keywords: coumarin · fluorescent probes · phosphatases · pK_a · ratiometric measurement

[1] G. Grynkiewicz, M. Poenie, R. Y. Tsien, *J. Biol. Chem.* **1985**, *260*, 3440–3450.
[2] a) J. P. Y. Kao, A. T. Harootunian, R. Y. Tsien, *J. Biol. Chem.* **1989**, *264*, 8171–8178; b) H. Iatridou, E. Foukaraki, M. A. Kuhn, E. M. Marcus, R. P. Haugland, H. E. Katerinopoulos, *Cell Calcium* **1994**, *15*, 190–198.
[3] R. Y. Tsien, T. J. Rink, M. Poenie, *Cell Calcium* **1985**, *6*, 145–157.
[4] a) A. Miyawaki, J. Llopis, R. Heim, J. M. McCaffery, J. A. Adams, M. Ikura, R. Y. Tsien, *Nature* **1997**, *388*, 882–887; b) G. Zlokarnik, P. A. Negulescu, T. E. Knapp, L. Mere, N. Burres, L. Feng, M. Whitney, K. Roemer, R. Y. Tsien, *Science* **1998**, *279*, 84–88.
[5] D. W. Moss, *Clin. Chem.* **1982**, *28*, 2007–2016.
[6] D. W. Moss, F. D. Raymond, D. B. Wile, *Crit. Rev. Clin. Lab. Sci.* **1995**, *32*, 431–467.
[7] S. Shenolikar, *Annu. Rev. Cell Biol.* **1994**, *10*, 55–86.
[8] T. R. Burke, Z. Y. Zhang, *Biopolymers* **1998**, *47*, 225–241.
[9] a) H. N. Fernley, P. G. Walker, *Biochem. J.* **1965**, *97*, 95–103; b) D. Robinson, P. Willcox, *Biochim. Biophys. Acta Enzymol.* **1969**, *191*, 183–186; c) J. M. Denu, D. L. Lohse, J. Vijayalakshmi, M. A. Saper, J. E. Dixon, *Proc. Natl. Acad. Sci. USA* **1996**, *93*, 2493–2498.
[10] a) B. Rotman, J. A. Zderic, M. Edelstein, *Proc. Natl. Acad. Sci. USA* **1963**, *50*, 1–6; b) Z. Huang, Q. Wang, H. D. Ly, A. Gorvindarajan, J. Scheigetz, R. Zamboni, S. Desmarais, C. Ramachandran, *J. Biomol. Screening* **1999**, *4*, 327–334.
[11] S. Welte, K.-H. Baringhaus, W. Schmider, G. Müller, S. Petray, N. Tennagels, *Anal. Biochem.* **2005**, *338*, 32–38.
[12] H. Takakusa, K. Kikuchi, Y. Urano, H. Kojima, T. Nagano, *Chem. Eur. J.* **2003**, *9*, 1479–1485.
[13] K. R. Gee, W. C. Sun, R. H. Bhalgat, R. H. Upson, D. H. Klaubert, K. A. Latham, R. P. Haugland, *Anal. Biochem.* **1999**, *273*, 41–48.
[14] Z. Huang, N. A. Olson, W. You, R. P. Hauglamd, *J. Immunol. Methods* **1992**, *149*, 261–266.
[15] a) G. G. Guilbault, J. Hieserman, *Anal. Chem.* **1969**, *41*, 2006–2009; b) J. P. Goddard, J. L. Reymond, *Trends Biotechnol.* **2004**, *22*, 363–370.
[16] D. W. Fink, W. R. Koehler, *Anal. Chem.* **1970**, *42*, 990–993.
[17] W. C. Sun, K. R. Gee, R. P. Haugland, *Bioorg. Med. Chem. Lett.* **1998**, *8*, 3107–3110.
[18] G. M. Huitink, D. P. Poe, H. Diehl, *Talanta* **1974**, *21*, 1221–1229.
[19] M. Adamczyk, M. Cornwell, J. Huff, S. Rege, T. V. S. Rao, *Bioorg. Med. Chem. Lett.* **1997**, *7*, 1985–1988.

Received: April 7, 2009
Published online on May 22, 2009

Zinc is an essential trace element for spermatogenesis

Sonoko Yamaguchi[a], Chiemi Miura[a], Kazuya Kikuchi[b], Fritzie T. Celino[a], Tetsuro Agusa[c,1], Shinsuke Tanabe[c], and Takeshi Miura[a,2]

[a]Research Group for Reproductive Physiology, South Ehime Fisheries Research Center, Ehime University, 1289-1, Funakoshi, Ainan, Ehime 798-4131, Japan; [b]Graduate School of Engineering, Osaka University, Osaka 565-0871, Japan; and [c]Center for Marine Environmental Science, Ehime University, Matsuyama 790-8577, Japan

Edited by Ryuzo Yanagimachi, University of Hawaii, Honolulu, HI, and approved May 8, 2009 (received for review January 19, 2009)

Zinc (Zn) plays important roles in various biological activities but there is little available information regarding its functions in spermatogenesis. In our current study, we further examined the role of Zn during spermatogenesis in the Japanese eel (*Anguilla japonica*). Human CG (hCG) was injected into the animals to induce spermatogenesis, after which the concentration of Zn in the testis increased in tandem with the progression of spermatogenesis. Staining of testicular cells with a Zn-specific fluorescent probe revealed that Zn accumulates in germ cells, particularly in the mitochondria of spermatogonia and spermatozoa. Using an in vitro testicular organ culture system for the Japanese eel, production of a Zn deficiency by chelation with *N,N,N′,N′*-tetrakis (2-pyridylemethyl)ethylenediamine (TPEN) caused apoptosis of the germ cells. However, this cell death was rescued by the addition of Zn to the cultures. Furthermore, an induced deficiency of Zn by TPEN chelation was found to inhibit the germ cell proliferation induced by 11-ketotestosterone (KT), a fish specific androgen, 17α,20β-dihydroxy-4-pregnen-3-one (DHP), the initiator of meiosis in fish, and estradiol-17β (E2), an inducer of spermatogonial stem-cell renewal. We also investigated the effects of Zn deficiency on sperm motility and observed that TPEN treatment of eel sperm suppressed the rate and duration of their motility but that co-treatment with Zn blocked the effects of TPEN. Our present results thus suggest that Zn is an essential trace element for the maintenance of germ cells, the progression spermatogenesis, and the regulation of sperm motility.

apoptosis | germ cells | in vitro culture | Japanese eel | sperm motility

Zinc (Zn) is well known as an essential trace element for a variety of biological activities. In biological systems, Zn is present in protein-bound and ionic forms, and plays important roles in mediating the function and structure of proteins, and in maintaining physiological balance. In vertebrates, Zn accumulates in the testis at high levels which are comparable to those in liver and kidney (1). In epidemiological studies in human, the inhibition of spermatogenesis and sperm abnormalities have been observed in patients with Crohn's disease and nutritional disorders, both of which induce a Zn deficiency (1–3). In vivo experiments in rodents have also demonstrated that a Zn deficiency can cause severe damage to the testes such as atrophy of the testicular tubules and the inhibition of spermatid differentiation (4, 5). Moreover, there are some reports that exposure to Zn can alleviate testis damage by stresses such as heavy metals, fluoride, and heat (6). These findings suggest that the testes may harbor a Zn-incorporation system, and that Zn itself may exert protective effect against testicular injury and play an essential role in the maintenance of testicular functions. However, there has been no evidence reported to date that shows any direct effects of Zn upon spermatogenesis in vertebrates.

In contrast to spermatogenesis, the effects of Zn on sperm motility have been examined in a number of vertebrate and invertebrate species. In humans, sperm motility declines in association with increased Zn concentrations in the seminal plasma (7). Morisawa and Yoshida have also reported that Zn in the seminal plasma of human suppresses sperm motility, and that the removal of Zn by binding to a protein named semenogelin enhances motility (6). On the other hand, in sea urchin, treatment with the bivalent metal ion chelator, ethylenediamine tetra acetic acid (EDTA), inhibits sperm motility that is reversed by the addition of Zn (9). These results suggest that extracellular Zn indeed affects sperm motility but whether this is inhibitory or stimulatory appears to be species-specific. Additionally, it has been reported that Zn is present in sperm mitochondria and flagella (10, 11) but there had been no reports to date concerning the role of intracellular Zn upon sperm function.

To further study the role of Zn upon spermatogenesis in our current study, we chose Japanese eel (*Anguilla japonica*) as our animal model. In the Japanese eel in vivo, a complete pathway of spermatogenesis, from the spermatogonia stage to sperm maturation, can be induced by the injection of human CG (hCG; 12). Furthermore, we have developed a testicular organ culture system for the Japanese eel in our laboratory, which is the only currently available system of its kind in which the induction of complete spermatogenesis can be performed in vitro by the addition of 11-ketotestosterone or hCG (13, 14). By in vivo and in vitro analyses of spermatogenesis in the Japanese eel, we have previously further clarified the regulatory mechanisms underlying fish spermatogenesis (15, 16). Additionally, we have revealed the inhibitory effects of 4 trace elements (lead, molybdenum, rubidium, and arsenic) on fish spermatogenesis using our in vitro testicular organ culture system (17). In our present study, we again used the Japanese eel model to investigate the concentration and distribution of Zn in testis during spermatogenesis. Moreover we examined the effects of Zn addition and deficiency on spermatogenesis and sperm motility in vitro.

Results

Changes in the Levels and Distribution of Zinc (Zn) in the Testis of the Japanese Eel during Spermatogenesis. Before injection with hCG, the concentration of Zn in the testis of the Japanese eel was approximately 50 μg/g. After injection, the Zn concentration in the testis gradually increased, and the highest levels were observed on day 9. Thereafter, the concentration of Zn remained at high levels until day 18 (Fig. 1).

To detect the distribution of Zn in eel testes, an unfixed testicular fragment was stained with a fluorescence sensor for Zn(II), ZnAF-2DA. Strong fluorescent signals were obtained in the lobules but not in the interstitial tissue (Fig. 2*A* and *B*). We thus further investigated the distribution of Zn in testicular tissue using isolated cells. Germ cells were found to be strongly stained

Author contributions: S.Y., C.M., and T.M. designed research; S.Y., C.M., F.T.C., T.A., S.T., and T.M. performed research; K.K. contributed new reagents/analytic tools; S.Y., C.M., and T.M. analyzed data; and S.Y., C.M., and T.M. wrote the paper.

The authors declare no conflict of interest.

This article is a PNAS Direct Submission.

[1]Present address: Faculty of Medicine, Shimane University, Izumo, Shimane 693-8501, Japan.

[2]To whom correspondence should be addressed. E-mail: miutake@agr.ehime-u.ac.jp.

PHYSIOLOGY

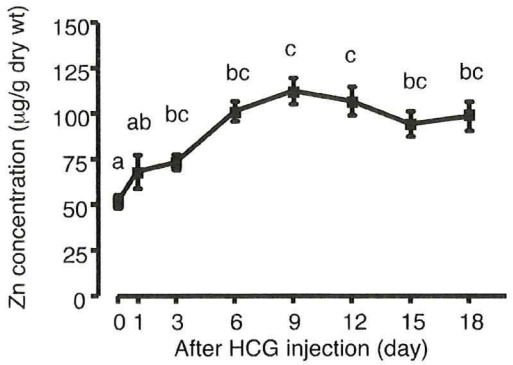

Fig. 1. Changes in the Zn concentrations in the testis of the Japanese eel after injection of human CG (hCG). The different letters indicate statistically significant differences ($P < 0.05$).

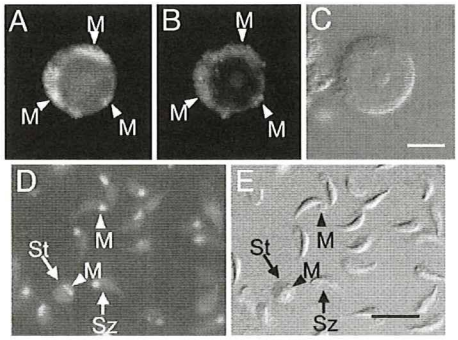

Fig. 3. Zinc distribution in germ cells of the Japanese eel. Zn was stained using ZnAF-2DA. Fluorescence images are shown for (*A*) Zn, and (*B*) mitochondria. (*C*) Bright field image of spermatogonia. (*D*) Zn fluorescence and (*E*) bright field image of spermatids and spermatozoa. M, mitochondria; St, spermatid; Sz, spermatozoa. (Scale bars: 10 μm.)

by ZnAF-2DA but Sertoli cells showed no signal (Fig. 2 *C* and *D*). When the germ cells were treated with 10 mM *N*,*N*,*N*′,*N*′-tetrakis(2-pyridylemethyl) ethylenediamine (TPEN) for 1 h before staining with ZnAF-2DA, fluorescence was not detected (Fig. 2 *E* and *F*). We also stained the germ cells at various stages with ZnAF-2DA, that is, spermatogonia, spermatocytes, spermatids, and spermatozoa. ZnAF-2DA signals were detectable in spermatogonia, most notably in the mitochondria (Fig. 3 *A*–*C*). Additionally, the mitochondria of the spermatids and spermatozoa also displayed strong ZnAF-2DA signals (Fig. 3 *D* and *E*).

Effects of Zn and Zn Chelators on Japanese Eel Testes in Vitro. To investigate the putative key role of Zn during spermatogenesis, we analyzed the direct effects of Zn on the testis in the presence or absence of 11-ketotestosterone (KT). After culturing for 6 days, testicular fragments in the control group were found to be occupied by type A spermatogonia. Although the histological structure of the testicular fragments cultured with KT alone did not differ from the control group, the incorporation ratio of BrdU into the germ cells had significantly increased (Fig. 4), as also reported in our previous study (13). Treatment of the Japanese eel testicular fragments with any level of Zn with or without KT did not affect the histology of the testis or the BrdU index (Fig. 4*A*). Treatment with ethylenediamine-*N*,*N*,*N*′,*N*′-tetraacetic acid, calcium(II), disodium salt (Ca-EDTA), an extracellular Zn chelator, also did not affect the BrdU index or testicular morphology after 6 days in culture (Figs. 4*B* and 5*B*). In contrast, exposure to 0.01 and 0.1 mM TPEN, an intracellular chelator of Zn, inhibited BrdU-incorporation into germ cells (Fig. 4*B*), and induced germ cell death (Figs. 4*B* and 5*C*). Significantly, both the cell death and the inhibition of BrdU incorporation induced by TPEN was rescued by the addition of Zn (Figs. 4*B* and 5*D*). We further investigated the type of cell death that occurred using a TdT-mediated dUTP nick-end

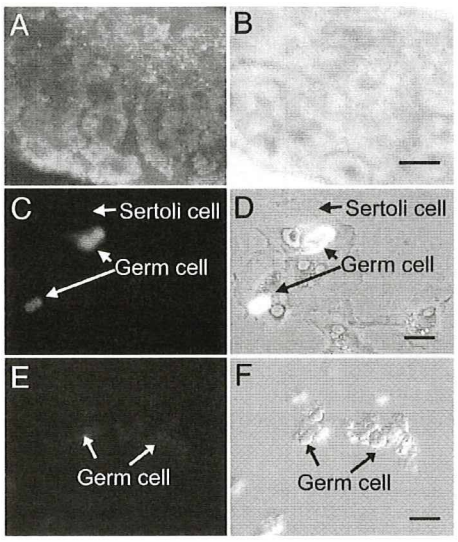

Fig. 2. The zinc distribution in the testis of the Japanese eel determined by staining with a Zn-specific fluorescent probe, ZnAF-2DA (*A*, *C*, and *E*). Bright field images are also shown (*B*, *D*, and *F*). (*A* and *B*) testicular fragments of the Japanese eel at 15 days after injection of hCG; (*C* and *D*) germ cells and Sertoli cells; (*E* and *F*) TPEN-treated germ cells. (Scale bars: *A* and *B*, 100 μm; *C*–*F*, 20 μm.)

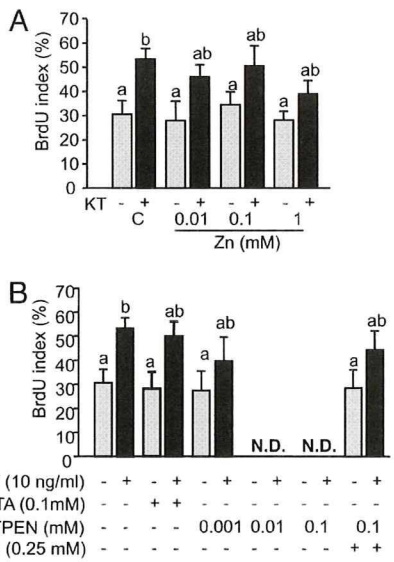

Fig. 4. Effects of Zn and Zn chelators on the early stages of spermatogenesis in vitro. The BrdU-labeling index was determined for germ cells in testicular fragments cultured with Zn (*A*) or Zn chelators (*B*) with or without KT. The number of BrdU-positive germ cells is expressed as a percentage of the total number of germ cells. C, control; Zn, $ZnCl_2$; KT, 11- ketotestosterone; TPEN, *N*,*N*,*N*′,*N*′-tetrakis(2-pyridylmethyl)ethylenediamine; CaEDTA, ethylenediamine -*N*,*N*,*N*′,*N*′- tetraacetic acid, calcium(II), disodium salt, dihydrate. Results are given as the mean ± SEM. The different letters on the columns indicate statistically significant differences ($P < 0.05$).

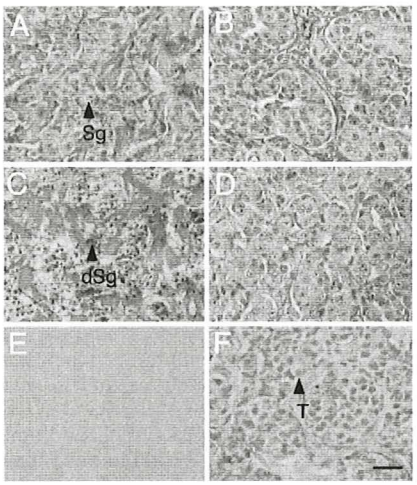

Fig. 5. Light micrographs of testicular fragments after culture with Zn chelators for 6 days. (*A–D*) Hematoxylin and eosin-stained testicular fragments cultured for 6 days. (*A*) control; (*B*) cultured with 0.1 mM CaEDTA; (*C*) cultured with 0.01 mM TPEN; (*D*) cultured with 0.1 mM TPEN and 0.25 mM $ZnCl_2$. (*E* and *F*) One-day cultures of testicular fragments subjected to a TUNEL assay. (*E*) control; (*F*) cultured with TPEN. Dark stained cells are TUNEL-positive (*E* and *F*). Sg, spermatogonia; dSg, dead spermatogonia; T, TUNEL-positive cells. (Scale bar: 20 μm.)

labeling (TUNEL) assay after a 1-day culture in the presence of TPEN. In the control and KT-treatment groups, no cell staining was observed (Fig. 5*E*). However, TUNEL-positive germ cells were detectable after treatment with 0.01–0.1 mM TPEN with or without KT (Fig. 5*F*).

We also investigated the effects of 0.001 mM TPEN, a dose that does not cause cell death, upon KT-induced spermatogenesis using our testicular organ culture system. Treatment with this dosage for 6 days had no effects on the histological structure of the testicular fragments. In contrast, after 15 days of this treatment, the testicular fragments were found to only have type A spermatogonia, although those cultured with KT alone contained the more progressed germ cells, type B spermatogonia (Fig. 6 *A–C*). Importantly, the addition of Zn led to a recovery of spermatogenesis, such that the TPEN/KT treated cultures resembled those exposed to KT alone (Fig. 6*D*).

Effects of Zn on the Germ Cell Proliferation Induced by Various Steroid Hormones. In the Japanese eel, KT, 17α,20β-dihydroxy-4-pregnen-3-one (DHP), and estradiol-17β (E2) induce DNA

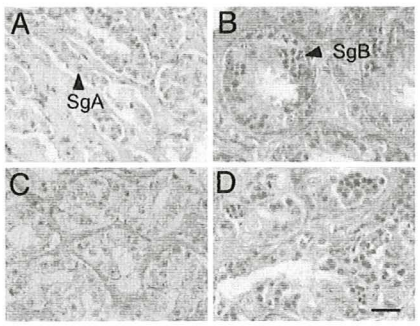

Fig. 6. Light micrographs of testicular fragments after culture with 10 ng/mL KT and 0.001 mM TPEN for 15 days. (*A*) Control; (*B*) cultured with 10 ng/mL KT; (*C*) cultured with KT and 0.001 mM TPEN; (*D*) cultured with KT, TPEN, and 0.0025 mM $ZnCl_2$. SgA, type A- spermatogonia; SgB, type B-spermatogonia. (Scale bar: 20 μm.)

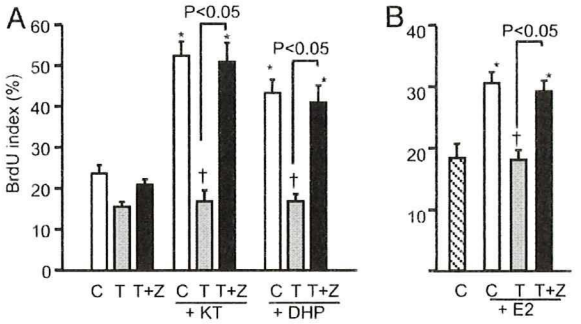

Fig. 7. Effects of a low dose TPEN upon germ cell proliferation in vitro. Testicular fragments were cultured with 0.001 mM TPEN and/or 10 ng/mL KT or DHP for 6 days (*A*) or cultured with TPEN and/or 1 ng/mL E2 (*B*). (*C*) Testicular fragments cultured without TPEN as a control for each steroid hormone; T, with TPEN; T+Z, with TPEN and Zn. KT, 10 ng/mL 11- ketotestosterone; DHP, 10 ng/mL 17α,20β-dihydroxy-4-pregnen-3-one; E2, 1 ng/mL estradiol-17β. Asterisks indicate significant differences from the negative control ($P < 0.05$). Daggers indicate significant differences from the control for each steroid hormone treatment ($P < 0.05$).

synthesis in germ cells thereby initiating spermatogenesis, meiosis, and spermatogonial stem-cell renewal, respectively (13, 16, 18). To elucidate at the stages of spermatogenesis at which Zn functions, that is, spermatogonial stem-cell renewal, spermatogonial proliferation or meiosis, we examined the effects of a 0.001 mM concentration of an intracellular Zn chelator on the germ cell proliferation induced by 10 ng/mL KT, 1 ng/mL E2, and 10 ng/mL DHP. These doses of KT, DHP and E2 were previously shown to be optimal for the induction of DNA synthesis in germ cells in vitro involving the initiation of spermatogenesis, meiosis, and spermatogonial stem-cell renewal, respectively (13, 16, 18). The rates of BrdU incorporation increased after treatment with KT and DHP for 6 days. However, treatment with 0.001 mM TPEN decreased the levels of BrdU incorporation induced by DHP or KT (Fig. 7*A*). To then investigate the effects of Zn on E2-induced germ cell proliferation, eel testes were cultured with E2 with or without 0.001 mM TPEN for 15 days according to the method of Miura et al. (18). Treatment with E2 alone significantly increased the number of BrdU-positive germ cells, whereas E2 in combination with 0.001 mM TPEN suppressed germ cell proliferation. This inhibition by TPEN was rescued by Zn treatment (Fig. 7*B*).

Effects of Zn Deficiency on Sperm Motility. In the mitochondria of Japanese eel sperm, strong ZnAF-2DA signals were observed. Hence, we analyzed the effects of Zn chelators on the rate and duration of eel sperm motility. Treatment of the sperm with Ca-EDTA did not alter their motility rate or duration at any concentration (Fig. 8*A* and *B*). In contrast, the addition of TPEN decreased both the motile rate and duration in a dose-dependent manner: 0.1–1 mM TPEN was found to be an effective concentration range for both indices. Furthermore, treatment with 1 mM Zn treatment rescued the inhibition of sperm motility by 1 mM TPEN (Fig. 8 *A* and *B*).

Discussion

Some previous studies have reported that a high concentration of Zn is detectable in testis, and that a Zn deficiency inhibits spermatogenesis and causes sperm abnormalities (5, 19). However, there are currently few reports that address the function of Zn during spermatogenesis in any detail. We thus investigated in our current study the distribution of Zn in testis and the direct effects of Zn upon spermatogenesis using an in vitro testicular organ culture model derived from the Japanese eel.

PHYSIOLOGY

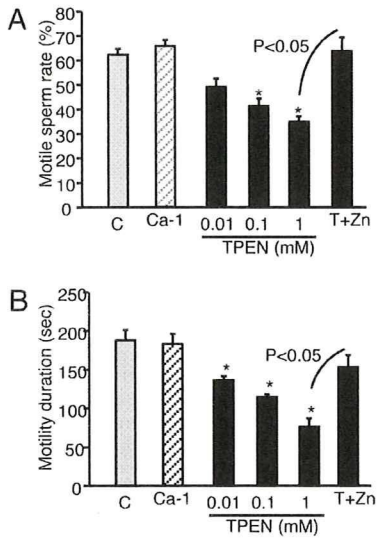

Fig. 8. Effects of Zn chelators on the motility of Japanese eel sperm. (*A*) Ratio of motile sperm; (*B*) duration of sperm motility. C, control; Ca-1, incubated with 1 mM Ca-EDTA; T+Z, incubated with 1 mM TPEN and 1 mM $ZnCl_2$. Asterisks indicate statistically significant differences from the control.

Our present analyses show that the Zn concentration in the testes of the Japanese eel gradually increases following an injection with hCG, and peaks on day 9 after this induction. Additionally, using a fluorescent Zn probe, strong signals were observed in germ cells, particularly spermatogonia, but not in the interstitial tissue or Sertoli cells. Similar to our present findings, Sørensen et al. have previously demonstrated by autometallography (AMG) that Zn is present in spermatogonia and primary spermatocytes in mouse (20). We previously demonstrated in our laboratory that a single injection of hCG first induced spermatogonial proliferation, then initiated meiosis on about day 12, and induced spermiogenesis on day 18 postinjection (12). Taken together therefore, our current data and previous findings suggest that Zn accumulates in the testis during early spermatogenesis, and may play a key role in the regulation of the spermatogonial proliferation and in the meiosis of germ cells. In the germ cells of other vertebrates, some Zn transporters have been observed. In rat, metallothionein (MT) was detected in spermatocytes (21) and other reports have shown that a testis-specific metallothionein-like protein (tesmin) is also present in these cells (22, 23). Additionally, Chi et al. have demonstrated that Zn accumulates in sperm in the mouse and that the Zn-exporter, ZnT-7, is present in the mouse testis, suggesting that Zn may be supplied to the germ cells via ZnT-7 (24). We speculate therefore that Zn may be accumulated in the germ cells of the Japanese eel via such transporter molecules.

In our present experiments in eel, Zn was found to accumulate prominently in the mitochondria in spermatogonia, spermatids and spermatozoa. In mouse, as detected via the AMG technique, sperm mitochondria were also previously shown to accumulate Zn, similar to our current results (10). Costello et al. have reported that Zn is imported into the mitochondria of prostate and liver cells in the form of a Zn-ligand complex such as Zn-citrate and Zn-MT (25, 26). Additionally, the membrane type Zn transporter protein ZnT-1 is expressed in the mitochondria of mouse spermatozoa (21). Taken together, there is now ample evidence to suggest that mitochondria may harbor a transporting system for Zn, and that Zn itself may have an important role to play in mitochondrial function in germ cells. In addition to mitochondria, Zn has also been detected in other areas of the cytoplasm in eel spermatogonia. In rat, Zn accumulates in the cytoplasm of both spermatogonia and spermatocytes (20). Furthermore, murine ZnT-7 is present in Golgi apparatus of spermacytes and spermatids (24). Thus, other organelles and cytosolic compartments may also accumulate Zn as part of its germ cell functions.

To further clarify the role of Zn in germ cells, we also investigated the effects of Zn and intra/extracellular Zn chelators on spermatogenesis using our in vitro testicular organ culture system develop from the Japanese eel. The results of these experiments demonstrated that treatment with the intracellular chelator TPEN caused germ cell death, which was blocked by the addition of Zn. This suggests that Zn is an essential trace element for the maintenance of germ cells. We performed a TUNEL assay using cultured testes and found that TPEN specifically caused apoptotic death in germ cells. There are some reports that a Zn deficiency causes apoptosis in various cell and tissue types. In human lymphocytes and rat hepatocytes for example, treatment with TPEN causes DNA fragmentation (27, 28). Interestingly, an in vitro and in vivo Zn deficiency was shown to induce caspase-3 activity in human mast cells and rat embryos, respectively (29, 30). Furthermore, treatment with Zn induces the antiapoptotic protein Bcl-2 and inhibits apoptosis in U947 cells (31). Caspase-3 and Bcl-2 in mitochondria have important roles in mitochondrial apoptosis; caspase-3 is released after cell damage and induces apoptosis, whilst Bcl-2 suppresses the apoptotic response (32). In our present study using a fluorescent Zn probe, we found that Zn accumulates in the mitochondria of germ cells and this may underpin its protection of these cells from apoptosis. However, the molecular mechanisms of how Zn regulates caspase-3 and Bcl-2 in mitochondria remain unclear at present. Some studies have addressed the correlation between Zn and apoptosis and suggest that Zn may function as an antioxidant in cells (32). Further studies will be necessary to clarify the role of Zn in the maintenance of germ cells.

We additionally investigated the influence of mild Zn deficiency on spermatogonial stem-cell renewal, spermatogonial proliferation, and meiosis in vitro. In a previous study, we reported that KT, E2, and DHP induce spermatogenesis, spermagonial stem-cell renewal, and meiosis in eel germ cells, respectively (13, 15, 16). In our present report, TPEN was found to inhibit all steroid hormone-induced DNA synthesis in the testes of the Japanese eel. These results suggest that Zn has an important role in DNA synthesis involving mitotic cell proliferation and meiosis. A previous study using 3T3 cells has reported that treatment with the Zn chelator, diethylenetriaminepentaacetic acid, decreases the mRNA expression and activity of thymidine kinase, after which DNA synthesis was inhibited in 3T3 cells (33). Furthermore, steroid hormone receptors such as progestin, androgen, and estrogen receptors all harbor Zn finger motifs within their structures (34). Other transcription factor genes containing Zn-finger motifs are also expressed during spermatogenesis (35). These findings suggest therefore that during steroid hormone-induced DNA synthesis, germ cells may incorporate Zn to activate a number of specific enzyme and Zn finger proteins, which are functionally disrupted by TPEN. Further analyses will be necessary to clarify the role of Zn on the functions of steroid hormone receptors and transcription factors during spermatogenesis.

Our current findings demonstrate that treatment with TPEN decreases sperm motility in the Japanese eel. Consistently in this regard, studies of human sperm have also demonstrated that diethyldithiocarbamate, which is an intracellular Zn chelator, inhibits sperm motility and decreases sperm velocity (36). These results suggest that intracellular Zn is important for sperm motility. As mentioned above, the mitochondria in the sperm of

the Japanese eel accumulate Zn. The ATP synthesized by the mitochondria is required for sperm flagella motility (37). Hence, Zn may have a function in mitochondrial ATP synthesis. Additionally, carbonic anhydrase (CA) is necessary for eel sperm motility, and this enzyme is expressed in the sperm membrane. CA catalyzes the reversible hydration of carbon and regulates the pH in various fluids. After spermiation, CA in the eel spermatozoa is activated after which it increases the pH and then induces sperm motility (15). CA is also known to be a Zn-binding protein, and its activity is dependent on the Zn concentration (38). Additionally, the removal of Zn from Zn-protein complexes extracted from human U87 human glioblastoma-astrocytoma cells by TPEN inhibited the function of the transcription factor, Sp1 (39). Although there is currently no information on effects of TPEN on CA activity, we speculate that TPEN may inhibit sperm motility by sequestering Zn away from this enzyme in sperm.

In conclusion, the results of our present study demonstrate that the Zn concentration in testis increases during spermatogenesis, and that Zn accumulates mainly in germ cells but not in either interstitial tissue or Sertoli cells. Our in vitro testicular organ culture experiments also demonstrated that a Zn deficiency causes the inhibition of DNA synthesis in germ cells, and induces an apoptotic response. Additionally, a Zn deficiency was found to suppress sperm motility in the Japanese eel animal model. These results suggest that Zn is an essential trace element for the maintenance and regulation of both spermatogenesis and sperm motility. However, the detailed mechanisms of Zn action during spermatogenesis remain to be clarified in further studies.

Materials and Methods

Animals. Cultivated male Japanese eels (180–200 g) were purchased from a commercial supplier and kept in a freshwater tank at 23 °C until use.

Measurement of Zn in Testis During Spermatogenesis. A previous report has indicated that hCG injection of a cultivated Japanese eel induces a complete cycle of spermatogenesis (11). Hence, these animals were injected with 1,000 IU/eel of hCG following anesthetization by ethylbenzoate. After injection, the fish were kept in a freshwater tank at 23 °C for 1, 3, 6, 9, 12, 15, and 18 days. Thereafter, hCG-injected eels (n = 5 for each day) were anesthetized and dissected, and the testes were collected and stored at −30 °C until measurement of Zn concentration. Before the experiments, testicular fragments were sampled from 5 uninjected eels as an initial control group. The testicular samples were dried for 12 h at 80 °C. For the analysis of Zn, dried testes were digested with HNO_3 in a microwave oven (ETHOS D, Milestone S.r.l.). The concentration of Zn was then measured using an inductively coupled plasma-mass spectrometer (ICP-MS; HP-4500, Hewlett-Packard).

Distribution of Zn in the Testis. We stained both the testicular fragments of the Japanese eel and the cells derived from these tissues with a Zn-specific probe. For this purpose, testis samples collected from the eels were cut into 100-μm sections in ice-cold eel Ringer's solution using a Vibratome 3000 (Vibratome). Testicular cells were also prepared according to Miura et al. (40, 13, 16) for Zn staining. Briefly, testes were harvested and testicular cells were isolated by collagenase and dispase treatments. After treatment with DNase I, testicular cells were cultured in plastic culture dishes at 20 °C overnight and both fibroblasts and interstitial cells were allowed to adhere to the bottom of the dish, thus separating these cells from germ cells and Sertoli cells. The germ cells and Sertoli cells were then collected from the culture dishes and plated in collagen-coated dishes at 20 °C overnight. After this overnight culture, only the Sertoli cells adhere to the bottom of the dish. Thereafter, germ cells were collected in a test tube, and both the germ cells and Sertoli cell preparations were used to analyze the Zn distribution. Sertoli cells and germ cells could be identified using a variety of distinguishing characteristics and specific marker expression. Sertoli cells attached and spread to the bottom of the dish, whereas germ cells did not attach and appeared spherical in shape. Furthermore, only germ cells express the progenstin receptor. We separated germ cells and Sertoli cells using this method previously (16).

Before staining of the germ cells, they were attached to a polyL-lysine coated glass slide. Testicular fragments, attached germ cells and Sertoli cells were then washed 3 times in eel Ringer's solution, and incubated with 1 μM of a permeable Zn-specific probe, Zn-AF 2DA (41) in eel Ringer's solution for 45 min at 20 °C. After this incubation, the cells were washed again in the Ringer's solution for 1 h at 20 °C and analyzed by fluorescence microscopy. The mitochondria of the spermatogonia were stained using MitoTracker Red (Invitrogen Co. Ltd.) according to the manufacturer's instructions with minor modifications before staining with Zn-AF 2DA.

In Vitro Testicular Organ Cultures. Organ cultures were prepared in accordance with the method of Miura et al. (13, 42). Male Japanese eels were dissected after anesthetization with ethylbenzoate. The testes were then collected, placed in ice-cold eel Ringer's solution and dissected into small pieces. Testicular fragments were placed on nitrocellulose membranes on top of cylindrical 1.5% agarose gels and set into a 24-well culture plate. Thereafter, 1 mL of Leibovitz' L-15 culture medium (Invitrogen Co. Ltd.) for eels (13) was added into each well with or without 0.01–1 mM $ZnCl_2$ (Zn), 0.001–0.1 mM TPEN, or 0.001–0.1 mM Ca-EDTA, which are intracellular and extracellular chelators of Zn, respectively, in combination with or without 10 ng/mL KT. The concentrations of Zn and chelators used in the in vitro experiments were based on the results obtained from the Zn measurement in the testis. Testicular fragments were incubated for 6 or 15 days and then fixed Bouin's solution for histological analysis.

Analysis of the Effects of a Mild Zn Deficiency upon Germ Cells. Testicular fragments were cultured with 0.001 mM TPEN in combination with 10 ng/mL KT, 1 ng/mL E2, and 10 ng/mL DHP for 6 or 15 days. Thereafter, testicular fragments were fixed and their histology was analyzed as described above.

Detection of Germ Cell Proliferation. The proliferation of Japanese eel germ cells was analyzed by immunohistochemical detection of 5-bromo-2-deoxyuridine (BrdU, Amersham Pharmacia Biotech) incorporation into replicating DNA. After culture for 6 or 15 days, testicular fragments were labeled with a 0.5 μl/mL BrdU solution for 18 h at 20 °C, and fixed in Bouin's solution. The fixed testicular fragments were then embedded in paraffin, cut into 4-μm sections, and subjected to immunohistochemistry with a mouse monoclonal anti-BrdU antibody.

TdT-Mediated dUTP Nick-End Labeling (TUNEL) Assay. For the detection of apoptosis, the TUNEL assay was performed. One-day cultured testicular fragments were fixed in Bouin's solution, cut into 5 μm-thick paraffin sections and then analyzed using an In Situ Cell Death Detection Kit (Roche Diagnostics, Ltd.) according to the manufacturer's instructions.

Effects of Zn on Sperm Motility. Eel sperm was collected after injection of the animals with hCG as described by Ohta et al. (43) and diluted 1:10,000 with artificial seminal plasma (149.3 mM NaCl, 15.2 mM KCl, 1.3 mM $CaCl_2$, 1.6 mM $MgCl_2$, and 10 mM $NaHCO_3$, adjusted to pH 8.2, see 43). The diluted sperm were then treated with 0.01–1 mM TPEN or 0.01–1 mM Ca-EDTA with or without 1 mM $ZnCl_2$ for 12 h at 4 °C. Thereafter, the sperm motility rate in seawater was measured as described previously (43). The duration of sperm motility was measured from 15 s after dilution in seawater until all movement had ceased completely.

Statistical Analysis. The results presented in this study are expressed as the mean ± SEM. In instances where the data did not distribute normally, these values were converted to a logarithmic scale. Differences between the means were analyzed by 1-way analysis of variance followed by a Bonferroni multicomparison test. Statistical analysis was performed using GraphPad Prism software (GraphPad Software Inc.). In all cases, significance was set at $P < 0.05$.

ACKNOWLEDGMENTS. This study was supported by Grants-in-Aid for Scientific Research and for Fellows from the Japan Society for the Promotion of Science (JSPS), and by the Global COE Program from the Ministry of Education, Culture, Sports, Science and Technology (MEXT) of the Japanese government.

1. Bedwal RS, Bahuguna A (1994) Zinc, copper, and selenium in reproduction. *Cell Mol Life Sci* 50:624–640.
2. El-Tawil AM (2003) Zinc deficiency in men with Crohn's disease may contribute to poor sperm function and male infertility. *Andrologia* 35:337–341.
3. Prasad AS (2008) Zinc deficiency. *British Med J* 326:409–410.
4. Mason KE, Burns WA, Smith JC (1982) Testicular damage associated with zinc deficiency in pre- and postpubertal rats: Response to zinc repletion. *J Nut* 112:1019–1982.